Article

Investigation of the Fuzzy Complex between RSV Nucleoprotein and Phosphoprotein to Optimize an Inhibition Assay by Fluorescence Polarization

Silva Khodjoyan [1], Deborha Morissette [1], Fortune Hontonnou [2], Luis Checa Ruano [3,4], Charles-Adrien Richard [2], Olivier Sperandio [3], Jean-François Eléouët [2], Marie Galloux [2], Philippe Durand [1], Stéphanie Deville-Foillard [1] and Christina Sizun [1,*]

[1] Institut de Chimie des Substances Naturelles, CNRS, Université Paris Saclay, F-91190 Gif-sur-Yvette, France
[2] Virologie et Immunologie Moléculaires, INRAE, Université Paris-Saclay, F-78350 Jouy-en-Josas, France
[3] Structural Bioinformatics Unit, Department of Structural Biology and Chemistry, Institut Pasteur, Université de Paris, CNRS UMR3528, F-75015 Paris, France
[4] Collège Doctoral, Sorbonne Université, F-75005 Paris, France
* Correspondence: christina.sizun@cnrs.fr

Abstract: The interaction between Respiratory Syncytial Virus phosphoprotein P and nucleoprotein N is essential for the formation of the holo RSV polymerase that carries out replication. In vitro screening of antivirals targeting the N-P protein interaction requires a molecular interaction model, ideally consisting of a complex between N protein and a short peptide corresponding to the C-terminal tail of the P protein. However, the flexibility of C-terminal P peptides as well as their phosphorylation status play a role in binding and may bias the outcome of an inhibition assay. We therefore investigated binding affinities and dynamics of this interaction by testing two N protein constructs and P peptides of different lengths and composition, using nuclear magnetic resonance and fluorescence polarization (FP). We show that, although the last C-terminal Phe_{241} residue is the main determinant for anchoring P to N, only longer peptides afford sub-micromolar affinity, despite increasing mobility towards the N-terminus. We investigated competitive binding by peptides and small compounds, including molecules used as fluorescent labels in FP. Based on these results, we draw optimized parameters for a robust RSV N-P inhibition assay and validated this assay with the M76 molecule, which displays antiviral properties, for further screening of chemical libraries.

Keywords: respiratory syncytial virus; phosphoprotein; nucleoprotein; replication complex; fuzzy complex; protein–protein interaction; PPI inhibition; nuclear magnetic resonance; fluorescence anisotropy; B-cyano BODIPYs

1. Introduction

Respiratory Syncytial virus (RSV) is the most common pathogen for acute pediatric low respiratory tract infections (ALRI) and bronchiolitis [1]. RSV is an important cause of death in infants in developing countries and a substantial burden on healthcare systems and hospitals worldwide. In 2005, RSV led to ~33 million RSV-associated ALRI episodes, 3 million hospitalizations and 55,000–199,000 deaths in children younger than 5 years [2,3]. RSV also represents a still underestimated risk of severe infection and mortality for immunocompromised and elderly persons [4].

There is still no licensed human RSV vaccine, even after more than 6 decades of research. The monoclonal antibody Palivizumab, which is not efficient against ongoing infection, has been administered for prophylaxis only to high-risk infants, due to high cost and limited efficacy [5–7]. Very recently Nirsevimab, a long-acting antibody for similar applications [8], was approved by the European Medicines Agency. More than 30 RSV prevention candidates are currently in clinical development [9,10]. The licensed therapeutic arsenal against RSV is even more limited. Ribavirin, a nucleoside analogue, has

a low therapeutic index and is only used for high risk patients. Several drug molecules, antibodies and a siRNA, targeting the fusion process or the viral replication and transcription machinery, have recently entered clinical trials [5,7,11,12]. Fusion inhibitors targeting the RSV F protein, like the small compounds JNJ-53718678 [13], BTA-C585 (clinical trial NCT02718937), GS-5806 [14], and the ALX-0171 nanobody [15] completed phase 2 clinical trials. The viral RNA polymerase inhibitor ALS-008176 [16] also completed a phase 2 trial. Although promising, these drugs elicit known resistances, which calls for alternatives and/or combination therapies.

RSV is a nonsegmented single-stranded negative-sense RNA virus of the *Mononegavirales* order, *Pneumoviridae* family, and *Orthopneumovirus* genus [17]. Its genome consists of an RNA molecule enchased in a sheath made of RSV nucleoprotein (N protein), forming a helical ribonucleoprotein complex termed nucleocapsid [18–20]. Replication of the viral genome as well as transcription of viral mRNAs are carried out by the viral RNA polymerase machinery. The apo polymerase consists of the RSV L protein, a large multifunctional catalytic subunit, and its essential co-factor, the RSV phosphoprotein (P protein). The P protein mediates recognition of the genomic material by the polymerase via direct binding to the N protein [21–23]. This interaction between P and N proteins was also found to drive the formation of cytoplasmic condensates, which are involved in RSV replication [24,25]. Although the primary function of RSV P protein consists of tethering the polymerase onto its template, P is a multifunctional protein with several binding partners. These properties are closely linked to its mainly disordered structure, outside a short central tetramerization domain P_{OD} (Figure 1A) [26–28]. The N-terminal domain of P (P_{NTD}) is nearly fully disordered and contains several short linear motifs that are recognized by different viral and cellular proteins [29]. Of note, the N-terminus of P is involved in the formation of the N^0-P complex, where P serves as a chaperone for RNA-free N protein (N^0) and maintains N competent for encapsidation of genomic RNA [30]. The C-terminal domain of P (P_{CTD}) contains a large transiently structured region with α-helical propensity ($P_{C\alpha}$) [27], which is the binding site of the RSV L protein [23]. The 35–40 amino acid long C-terminal tail (P_{Ctail}) is fully disordered, and the 10 last amino acids were reported to be involved in the N-P interaction relevant for the holo polymerase complex [21,26,31].

The RSV N protein is an RNA-binding protein. When overexpressed as a recombinant protein in *E. coli*, N binds to bacterial RNA and forms ring-shaped N-RNA complexes comprising 10–11 N protomers (Figure 1B) [32]. The N protein consists of two globular N-and C-terminal domains, N_{NTD} and N_{CTD}, connected by a hinge, where RNA binds (Figure 1B). These two domains are flanked by flexible N- and C-terminal arms. The N-terminal arm (35 residues) engages into inter-protomer interactions in N-RNA rings [32]. N_{NTD} contains the binding site of P_{Ctail} [21].

In contrast to full-length N, recombinant N_{NTD} is produced as a monomeric and RNA-free protein. We previously provided a high resolution structural basis for the N-P interaction with X-ray crystal structures of complexes between N_{NTD} and C-terminal P peptides, notably with the 2-mer $Asp_{240}Phe_{241}$ (P_2 peptide in Figure 1A,C) [33]. The C-terminal Phe_{241} residue of P_2 is anchored into a hydrophobic pocket at the surface of N (Figure 1C). Strikingly, for longer peptides, only this Phe_{241} residue was ordered in the crystal structures and adopted a well-defined position (Figure 1C). Nevertheless, there is evidence that the N-binding region of P extends beyond Phe_{241} in P_{Ctail}. A minigenome assay showed that in vitro replication of RSV was attenuated for the single $Leu_{238}Ala$ and the double $Glu_{239}Ala/Asp_{240}Ala$ P mutants [21]. This result is in line with in vitro binding assays performed with recombinant N protein and GST-fused P mutants, which showed that up to 9 C-terminal P residues are necessary for N-binding [31]. This was corroborated by affinity measurements carried out by NMR with two C-terminal P peptides, P_2 and the 12-mer P_{12} (Figure 1A). P_{12} displayed a 100-fold lower dissociation constant K_d (54 ± 9 µM) than P_2 (4.2 ± 1 mM) [33]. We hypothesized that P_{Ctail} could make multiple contacts with the surface of N, increasing avidity of P and contributing to affinity. Since the position of these contacts is not well defined, N_{NTD}-P_{CTD} can be considered as a fuzzy

complex [34,35]. Electrostatic interactions between the highly acidic P_{Ctail} and positively charged residues that are exposed at the surface of N around the P-binding pocket likely provide additional binding contribution. In cells, the negative charge of P_{Ctail} is increased by constitutive phosphorylation of the Ser_{232} and Ser_{237} residues [36–39]. Phosphorylation was shown to modulate RSV replication in vivo [39]. However, the Ser_{232} phosphorylation site was reported to be dispensable for viral RNA transcription and virus replication in vitro [36,38,39].
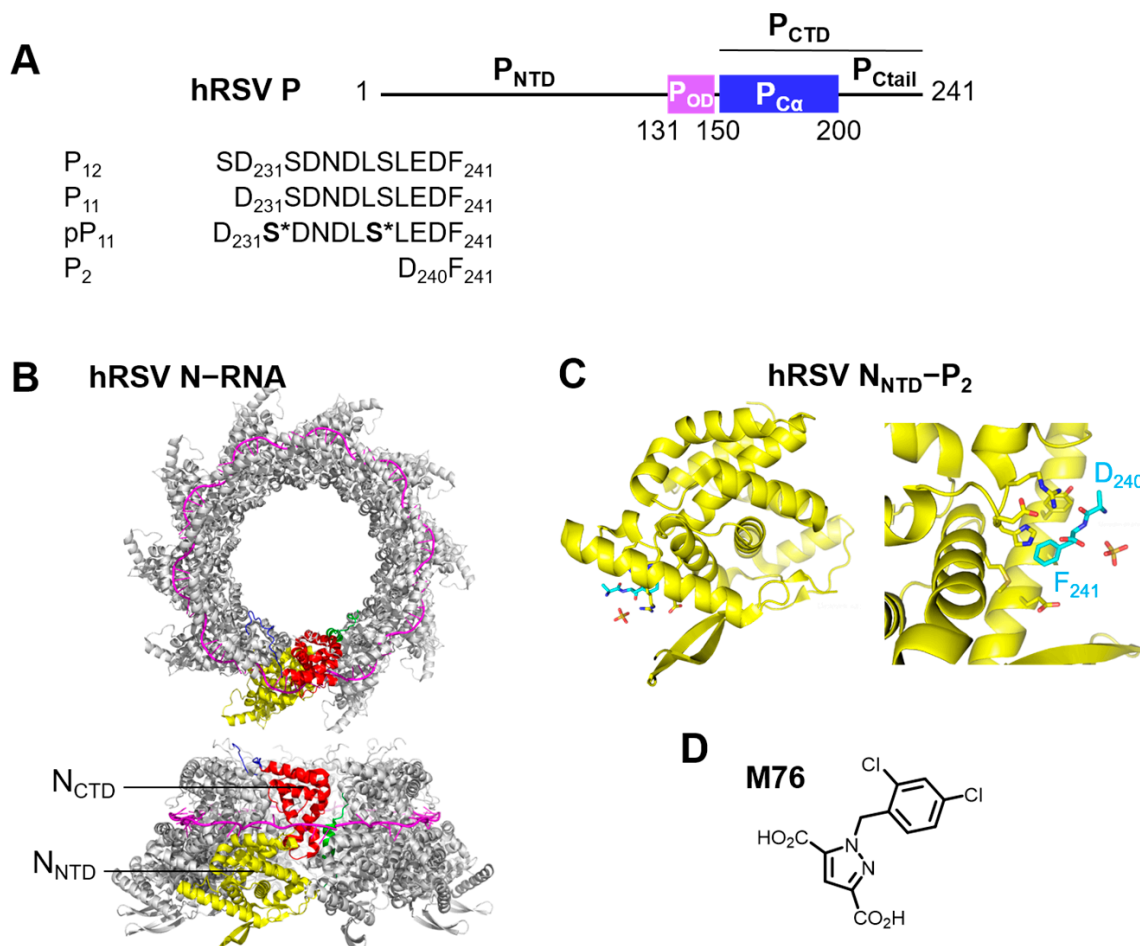

Figure 1. Human Respiratory Syncytial Virus (hRSV) phosphoprotein P and nucleoprotein N. (**A**) Domain organization of the RSV P protein (NTD; N-terminal domain, OD; oligomerization domain, CTD; C-terminal domain, itself divided into an α-helix-rich domain Cα and a disordered C-terminal tail, Ctail) and amino acid sequence of C-terminal P peptides. Phosphorylated serines are marked by *. (**B**) Two views of the X-ray crystal structure of an RSV N-RNA ring containing 10 N protomers (PDB 2wj8) in cartoon representation. The 7-mer RNA molecules are in magenta. One protomer is highlighted in color: N-terminal domain (N_{NTD}) in yellow, C-terminal domain (N_{CTD}) in red, N-terminal arm in green, C-terminal arm in blue. (**C**) Cartoon representation of the X-ray crystal structure of RSV N_{NTD} (yellow) in complex with the C-terminal P_2 peptide (cyan sticks) (PDB 4uc9). (**D**) Structure of M76 that inhibits the RSV N_{NTD}-P_{CTD} interaction.

Since the N_{NTD}-P_{CTD} interaction is essential for the formation of the viral holo RNA polymerase complex and hence for RSV replication, we proposed that the RSV N_{NTD}-P_{CTD} protein-protein interaction (PPI) could be a new drug target for PPI inhibitors. We previously showed that P_{CTD} could be displaced in vitro from N_{NTD} by 1-benzyl pyrazole 3,5-dicarboxylate derivatives, which mimic the sidechain and C-terminal carboxylate of Phe_{241} (Figure 1C) [33]. After chemical modification to improve its membrane passage, the M76 molecule (Figure 1D) was able to inhibit replication of recombinant fluorescent RSV

in cells. Results from other groups reinforce this hypothesis. Hesperitin, a flavanone that reduced intracellular RSV replication [40], was also shown to bind to the P-binding pocket of N_{NTD} and to compete with the 11-mer P_{11} peptide [41]. The EDP-938 benzodiazepine, which demonstrated antiviral activity, elicited mutations on N close to the P-binding pocket, suggesting that it might be an N-P inhibitor [42].

Hesperitin and M76, which compete with P for N-binding in vitro and display antiviral activity [33,40,41], were identified from a limited set of molecules and different screening approaches: hesperitin was identified from a flavonoid series using an antiviral assay, whereas M76 was obtained from a subset of the ZINC database selected in silico with a stringent filter based on chemical structure. High-throughput screening (HTS) of chemical libraries would enable to more widely explore the potential of the RSV N_{NTD}-P_{CTD} PPI as an antiviral target. This requires a relevant model of the interaction combined to a robust HTS method. We have shown previously that the complex between N_{NTD} and short C-terminal P peptides, derived from P_{Ctail}, affords a minimal complex mimicking the interaction between the P protein and the RSV nucleocapsid [33]. Fluorescence anisotropy (FA) [43], or equivalently fluorescence polarization (FP) (see Materials and Methods), are compatible with HTS [44]. FP has already been applied in the case of the RSV N-P interaction to probe inhibition by hesperitin [41] and by P_{Ctail}-derived peptides [45]. These FP measurements were performed under different experimental conditions, notably with different N protein constructs, different P peptides and different fluorescent labels. In this context, our aim was to obtain a deeper insight into the experimental requirements of an FP assay specific of the RSV N-P interaction. This led us to analyze the fuzzy complex formed between the N protein and the flexible P_{Ctail}.

2. Results

2.1. Phosphorylation of an RSV P_{Ctail}-Derived Peptide Increases Affinity for RSV N_{NTD}

We previously analyzed the RSV N_{NTD}-P_{12} complex using Nuclear Magnetic Resonance (NMR) [33]. As the isoelectric point of N_{NTD} is 7.8, we used MES pH 6.5 buffer to ensure the stability of the protein. This pH is also suitable for amide-detected 2D NMR experiments. The buffer contained salt (250 mM NaCl) to further stabilize N_{NTD} at protein concentrations required for NMR (50–100 µM). Under these experimental conditions we determined a K_d of 54 µM.

Here, as P protein is constitutively phosphorylated on Ser_{232} and Ser_{237} residues in cells, we first investigated the impact of phosphorylation on the affinity of the N_{NTD}-P_{Ctail} complex. We performed an NMR titration experiment by adding increasing amounts of pP_{11} peptide, where Ser_{232} and Ser_{237} residues were replaced by O-phosphoserines (pSer, Figure 1A), to a solution of ^{15}N-labeled N_{NTD}, and measured 2D ^1H-^{15}N HSQC spectra (Figure 2A). We worked in the same buffer as with P_{12}. At pH 6.5, the pSer sidechains are expected to be mostly negatively charged [46]. Addition of pP_{11} induced perturbations in the HSQC spectrum of N_{NTD}, in particular chemical shift perturbations (CSPs). Saturation of this effect was reached after addition of ~6 molar equivalents of peptide. At this peptide:protein ratio, the protein can be considered to be in a fully bound form. We measured combined ^1H and ^{15}N amide CSPs (Equation (1)) for N_{NTD} signals in a fast chemical exchange regime, i.e., signals that shifted in the spectrum without broadening at intermediate titration points (e.g., Ile_{129} in Figure 2A). Significant CSPs were located in and around the P-binding pocket, confirming that pP_{11} binds to the previously determined P-binding epitope on N_{NTD} (Figure 2B,C) [33]. We fitted the NMR titration curves of these residues with a single site binding model to determine residue-specific K_ds (Equation (2)), and calculated a mean K_d of 17.0 ± 4.5 µM from 26 individual values. Compared to the unphosphorylated P_{12} peptide, this represents a ~3-fold gain in affinity, which confirms the role of negative charges in P_{Ctail} for N-binding. Since measurements were made in a buffer with high ionic strength, the gain remains rather modest due to charge screening.
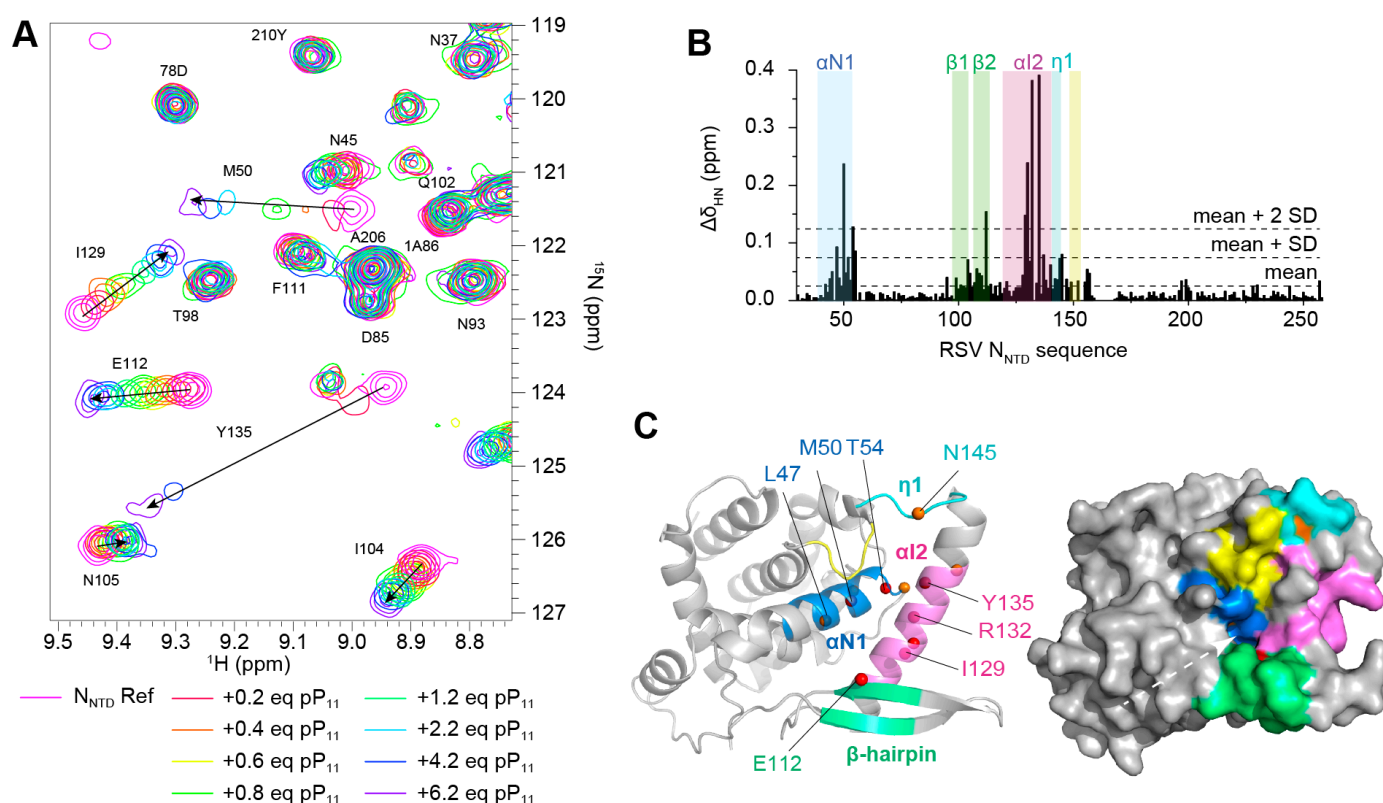
Figure 2. Binding of RSV pP$_{11}$ peptide to RSV N$_{NTD}$ protein followed by NMR. (**A**) Selected region of superimposed ^{1}H-^{15}N HSQC spectra of 50 μM ^{15}N-labeled N$_{NTD}$, in 20 mM MES pH 6.5, 250 mM NaCl buffer, recorded during a titration experiment with the pP$_{11}$ peptide. The magnetic field was 14.1 T, and the temperature 20 °C. The color code corresponds to the pP$_{11}$:N$_{NTD}$ molar ratio as indicated below the spectrum. (**B**) Bar diagram of combined amide chemical shift perturbations ($\Delta\delta_{HN}$) measured for N$_{NTD}$ in the presence of 4.2 molar equivalents of pP$_{11}$. Regions with significant CSPs are highlighted with a colored background: C-terminus of the αN1 helix (blue), β-hairpin (green), center of the αI2 helix (magenta), η1 loop (cyan), H$_{151}$-loop (yellow). (**C**) Mapping of CSPs onto the X-ray structure of N$_{NTD}$ (PDB 4ucc): amide nitrogen atoms are represented as red spheres for residues with $|\Delta\delta_{HN}|$ > mean + 2 SD, and orange spheres for $|\Delta\delta_{HN}|$ > mean + SD. The color code is the same as in (**B**). The same view in surface representation highlights the P$_{CTD}$ binding pocket, indicated by a white arrow.

Overall, signals of bound N$_{NTD}$ were broader than those of unbound N$_{NTD}$ (Figure 2A). This can be explained by the increase of molecular weight, when the complex is formed. Line broadening at saturation was more marked for residues belonging to the P-binding site, suggesting exchange phenomena as additional sources of broadening. They may reflect local mobility of P in the complex and intermediate binding states. Some N$_{NTD}$ signals with large chemical shift differences between bound and unbound states (e.g., Y$_{135}$ in Figure 2A) were broadened at intermediate titration points. Signals were recovered when saturation was reached, indicating that they are in an intermediate exchange regime. These residues were also located in or in the close vicinity of the P-binding pocket, and thus report on the same binding mode as residues in fast exchange. From chemical shift differences measured for these residues we determined an exchange rate k$_{ex}$ of ~800 s^{-1} (from Equation (3)) between free and bound N$_{NTD}$, which indicates a fast dynamic process. Since k$_{ex}$ (k$_{off}$ + k$_{on}$ × [N$_{NTD}$]) is a combination of association (k$_{on}$) and dissociation (k$_{off}$) rates, the relative contributions of dissociation and association could not be assessed by this method.

2.2. Fluorescence Polarization Reveals a Potential Secondary Binding Site on RSV N_{NTD} for Fluorescein-Labeled RSV P_{11} Peptide

2D Protein-observed NMR is a powerful tool that gives detailed structural and thermodynamic insight, but requires large sample amounts and is time-consuming. Acquisition of a single titration point in Figure 2 took 15 min. It is therefore not adapted for medium to high-throughput assays. Fluorescence polarization (FP) is more time-effective. FP is routinely used in screening assays for binding inhibitors [43,44,47,48]. We thus tested if we could transpose the experimental NMR conditions to FP measurements. We first wondered if the N_{NTD} construct, used for NMR, but also previously for isothermal titration calorimetry and surface plasmon resonance (SPR) experiments [33], was adapted for FP. As a general rule, fluorescence polarization increases with the apparent size of a fluorescent molecule. According to Perrin's equation (Equation (5)), the theoretical FP of fluorescein (fluorescence lifetime ~4 ns) bound to N_{NTD} (26.2 kDa) is ~400 mFP. This is close to 500 mFP, the theoretical maximal FP value, and indicates that the size of N_{NTD} is compatible with an FP assay.

We started by labeling the pP_{11} peptide with N-terminally attached BODIPY FL, as described by Shapiro at al. [45]. However, we observed that the BODIPY FL-labeled peptide (BF_2pP_{11}) was prone to degradation, either via peptide bond cleavage or BODIPY FL-defluorination, under slightly acidic conditions. We then produced F_{11}, another labelled peptide P_{11}, by changing the fluorescent label to fluorescein-5-thiourea (FTU) by coupling with fluorescein-5-isothiocyanate (FITC). F_{11} proved to be stable. It is similar to the 6-carboxyfluorescein P peptide used by Sa et al. for competition with hesperitin [41]. To directly compare FP and NMR data, we made measurements in MES pH 6.5 buffer. Brij-35 detergent (0.01% w/v) was added below its critical micellar concentration (0.11% w/v) to prevent spurious binding of the peptide to the reading plates. To determine the binding affinity of F_{11} peptide for N_{NTD}, we measured FP for 200 nM F_{11} by varying the concentration of N_{NTD}, which ranged from 0.1 to 120 µM (Figure 3A). We tested buffer with and without salt.
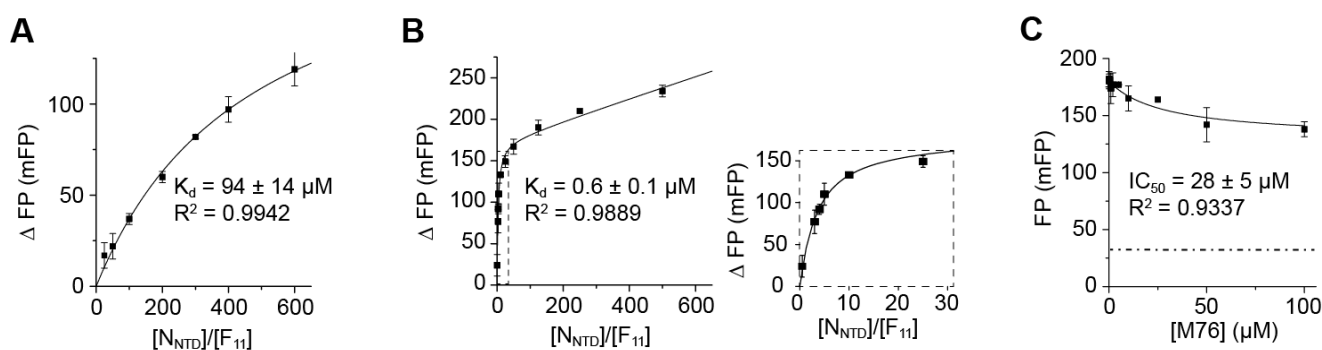

Figure 3. Binding of F_{11} to RSV N_{NTD} and inhibition by M76 assayed by fluorescence polarization. The buffer was MES pH 6.5, with 250 mM NaCl or without salt. The concentration of the fluorescent probe was 200 nM. (**A**) Binding of N_{NTD} to F_{11} in buffer with salt: ΔFP = FP − FP_{min} (the FP of free F_{11} was FP_{min} = 30 mFP) was plotted as a function of the N_{NTD}:F_{11} molar ratio. Error bars represent the difference between duplicate experiments. Data were fitted with a single site binding model (straight line) using K_d and ΔFP_{max} as parameters. R^2 indicates the quality of the fit. (**B**) Binding of N_{NTD} to F_{11} in salt-free buffer assayed by ΔFP. The area in the dotted contour box is expanded on the right side. Data were fitted with a single binding site model and an additional linear contribution. (**C**) Inhibition of N_{NTD} (5 µm) binding to F_{11} by the M76 Molecule in salt-free Buffer. FP data were fitted with a Hill Equation. IC_{50} and R^2 values are indicated. The dashed line indicates the mean FP value of free F_{11}.

In the presence of salt, FP measurements were stable for incubation times up to 48 h. FP of free F_{11} was 30–40 mFP. We fitted the binding curves with a single site binding model (Equation (10)). This yielded a maximal FP difference between bound and free F_{11} peptide

ΔFP_{max} = 210–230 mFP and a dissociation constant K_d = 90 ± 15 µM (Figure 3A). Saturation of the binding curve could not be obtained within the applied N_{NTD} concentration range, and this may induce an error on K_d determination. However, the K_d has the same order of magnitude as that determined by NMR for the P_{12} peptide under similar buffer conditions (K_d = 54 µM) [33]. The experimental FP_{max} value was lower than the theoretical value (~400 mFP), suggesting that the fluorescent label displays some mobility with respect to the complex. As the label is attached to the N-terminus of the peptide and hence to the opposite side of the anchoring Phe_{241} residue, this would be in line with a fuzzy N_{NTD}-P_{CTD} complex, where only the C-terminal Phe_{241} residue is well bound, whereas the rest of the P peptide remains disordered and only loosely attached.

In buffer without salt and in the presence of N_{NTD}, F_{11} FP stabilized only after 30 min. Binding curves were obtained, but the FP data did not reach a plateau at high N_{NTD} concentration. Instead, FP displayed a linear dependence with increasing N_{NTD}:F_{11} molar ratios, suggesting a second binding mode with low affinity (Figure 3B). We fitted the curves with a combination of a single binding site for the first mode and a linear contribution for the second mode. This yielded ΔFP_{max} = 175 mFP and K_d = 0.6 ± 0.1 µM. ΔFP_{max} was of the same order of magnitude in buffers with and without salt, indicating that the dynamic range of FP was not affected by salt. This suggests that the dynamics of the fluorescent probe were similar in these two conditions. In contrast, the affinity was significantly higher in the absence of salt, by 2 orders of magnitude, confirming the importance of electrostatic interactions for the N_{NTD}-P_{11} complex.

We previously showed by SPR that the M76 molecule (Figure 1D) could compete with P for N_{NTD} binding in vitro [33]. We therefore tested competition between M76 and F_{11} by FP. Measurements were done in salt-free buffer to take advantage of the higher F_{11}-N_{NTD} affinity. The concentration of N_{NTD} was set to 5 µM to benefit from a high range of FP values, comprised between FP_{min} and ~80% FP_{max} [48]. With increasing M76 concentration (up to 100 µM), F_{11} FP progressively decreased due to F_{11} displacement from N_{NTD} by M76 (Figure 3C). However, even at high M76 concentration, FP did not reach the FP_{min} value. Saturation occurred at a high FP of ~105 mFP, suggesting that M76 was not able to fully displace F_{11}. This corroborates the hypothesis of a secondary binding site on N_{NTD}, for which M76 does not compete. We fitted the data with a Hill equation (Equation (12)), assuming that the maximal inhibition of F_{11} binding to the canonical site by M76 was obtained at saturation. We obtained an IC_{50} of 28 ± 5 µM. This was converted into an inhibition constant K_i of 2.5 µM using the IC50-to-Ki server [49], assuming a competitive mechanism and following values: K_d = 0.6 µM for F_{11}, [N_{NTD}] = 5 µM, and [F_{11}] = 0.2 µM.

2.3. The Complex betweeen Fluorescein-Labeled C-Terminal P Peptides and Full-Length N Protein Provides a Robust Model of the RSV N-P Interaction for FP Measurements

As the FP data obtained with N_{NTD} in salt-free buffer suggest the existence of a secondary binding site, we wanted to test if this was still the case with full-length RSV N protein. Wild-type N is produced in the form of ring shaped N-RNA complexes by overexpression in *E. coli* [32]. These rings mimic one turn of the helical nucleocapsid, which is the natural partner of P_{Ctail}. We therefore chose to test N-RNA as an alternative N form. N-RNA complexes contain 10–11 protomers and 7 ribonucleotides per N protomer [32]. Due to the high molecular weight of N-RNA rings (~0.5 MDa), a high fluorescence polarization is expected.

We carried out FP measurements using the fluorescent F_{11} peptide and N-RNA complex. As N-RNA is more stable at pH 8.0 than at pH 6.5, we worked in Tris buffer. No salt was added to promote high affinity. The FP binding data could be fitted with a single site binding model (Figure 4A). We obtained ΔFP_{max} = 125–130 mFP, which is less than determined with the N_{NTD} construct, but again confirms the relative mobility of the fluorescent label. We determined a K_d of 7.6 ± 0.9 µM. Surprisingly, the K_d value obtained with N-RNA was one order of magnitude higher than with N_{NTD} (0.6 µM), suggesting that binding to N_{NTD} may not fully recapitulate binding to N-RNA.
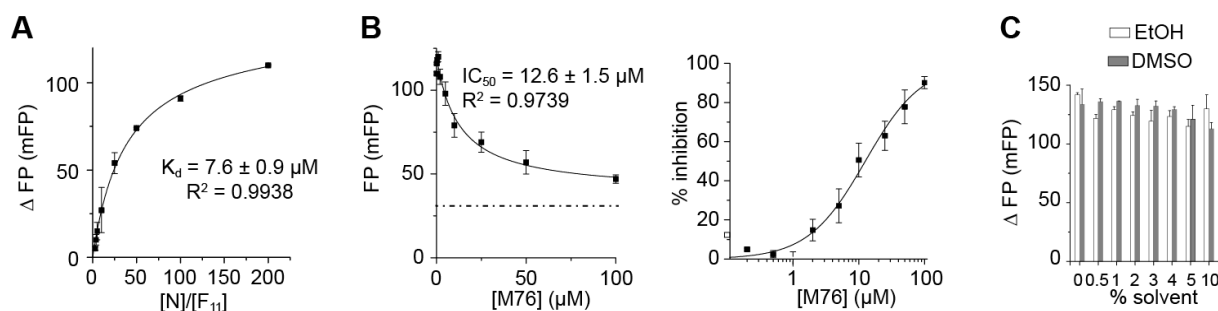
Figure 4. Binding of F_n peptides to RSV N-RNA complex and inhibition by M76 assayed by fluorescence polarization. The buffer was Tris pH 8.0 without salt. The concentration of fluorescent probe was 200 nM. (**A**) Binding of N-RNA to F_{11} was assayed by ΔFP as a function of the N:F_{11} molar ratio. Data were fitted with a single site binding model. (**B**) Inhibition of N-RNA (10 μM) binding to F_{11} by M76: The left hand panel represents the experimental FP data, and the right hand panel the percentage of inhibition, calculated assuming FP_{max} = 120 mFP and FP_{min} = 40 mFP. (**C**) Influence of solvent addition on ΔFP measurements for the F_{7E} peptide in the presence of N-RNA.

We next performed inhibition experiments for the F_{11}-(N-RNA) complex by M76 (Figure 4B). FP values decreased with increasing competitor concentration. At saturation, FP nearly reached the value of free F_{11}, showing that the F_{11} peptide could be nearly completely displaced. Since the same concentration range was used for N_{NTD} and N-RNA, poor solubility of M76 can be ruled out to explain the saturation observed before complete displacement of F_{11} in the presence N_{NTD} (Figure 3C). This reinforces the hypothesis of a second binding site on N_{NTD}, outside the canonical P-binding site. We fitted an IC_{50} of 12.6 μM (Figure 4B), which converts into a K_i of 2.4 μM (using K_d = 7.6 μM for F_{11}, [N] = 10 μM and [F_{11}] = 0.2 μM). The inhibition constant is similar to that obtained with N_{NTD} in salt-free buffer, which suggests that M76 binds in a similar way to the P-binding site on N_{NTD} and N-RNA.

M76 was dissolved in organic solvent such as ethanol or DMSO. This may affect the stability of the protein. We thus run a control experiment to evaluate the effect of solvent on FP measurements. We used the FTU-P_{7E} peptide F_{7E} (Table 1). Addition of up to 10% ethanol did not significantly affect FP measurements (Figure 4C). A slight decrease of FP was observed with 10% DMSO, but overall the FP assay is robust with respect to solvent. In summary, the N-RNA form appears to be suitable for FP measurements, as only specific binding of fluorescent P peptide and efficient inhibition by the M76 molecule were observed.

Table 1. FTU-labeled RSV P peptides (F_n) designed for fluorescence polarization measurements with RSV N-RNA and binding parameters obtained from FP curve fits. ϕ designates the FTU label. Phosphomimetic peptides, where Ser$_{232}$ and/or Ser$_{237}$ were mutated into glutamates, are annotated with the letter E. FP measurements were done with 200 nM fluorescent probe in Tris pH 8.0 buffer without salt. K_d and ΔFP_{max} were determined by fitting binding curves to a single site binding model or a combination with a linear contribution (lines marked with *).

F_n Peptide	Peptide Sequence	K_d (μM)	ΔFP_{max} (mFP)
F_{11}	ϕ-DS$_{232}$DNDLS$_{237}$LEDF-OH	7.6 $\pm$ 0.9	130 $\pm$ 5
F_{11EE}	ϕ-DE$_{232}$DNDLE$_{237}$LEDF-OH	0.38 $\pm$ 0.12/0.15 $\pm$ 0.12 (*)	114 $\pm$ 6/93 $\pm$13 (*)
F_{11SE}	ϕ-DS$_{232}$DNDLE$_{237}$LEDF-OH	0.87 $\pm$ 0.26/0.62 $\pm$ 0.25 (*)	111 $\pm$ 9/97 $\pm$ 12 (*)
F_{9E}	ϕ-DNDLE$_{237}$LEDF-OH	2.2 $\pm$ 0.3	148 $\pm$ 5
F_{7E}	ϕ-DLE$_{237}$LEDF-OH	2.5 $\pm$ 0.3	187 $\pm$ 7
F_{5E}	ϕ-E$_{237}$LEDF-OH	5.9 $\pm$ 0.5	285 $\pm$ 7
F_4	ϕ-LEDF-OH	35 $\pm$ 4	291 $\pm$ 20
F_3	ϕ-EDF-OH	62 $\pm$ 19	315 $\pm$ 61

2.4. Measurement of the Binding Affinity of RSV Fluorescein-P Peptides for RSV N-RNA and Influence of Peptide Length on Fluorescent Label Mobility

Fluorescent labels can only be attached to the N-terminus of the P peptides, since the C-terminus of P directly anchors onto the N protein via the Phe_{241} residue (Figure 1C). Since C-terminal P peptides are flexible [26], the fluorescent label displays relative mobility, as reflected by the moderate ΔFP_{max} values reported in the previous paragraphs. This raises the question about how the P peptide length impacts binding affinity and FP_{max}. We thus designed a series of eight P peptides with increasing length, from 3 to 11 amino acids, and labeled them with FTU (Table 1). Moreover, to investigate the effect of phosphorylation, we produced phosphomimetic peptides, where either Ser_{237} alone or both Ser_{232} and Ser_{237} were replaced by glutamates.

We first measured binding of F_n peptides (200 nM) to N-RNA in Tris buffer by FP (Figure 5A,B). For F_n peptides with $n \geq 5$, saturation of fluorescence anisotropy could be reached within the concentration range used for N-RNA, i.e., with 40 μM of total N protein concentration. The fully bound state of F_3 and F_4 peptides could not be obtained. We fitted the data with ΔFP_{max} and K_d as parameters. We observed that ΔFP_{max} decreased with the length of the peptide (Table 1), indicating that the dynamics of the fluorophore increase with its distance to the Phe_{241} anchor. Concomitantly, the affinity of F_n peptides increased with peptide length: K_ds decreased from 62 μM (F_3) to <1 μM (F_{11SE}) (Table 1), highlighting the contribution of residues other than the two C-terminal P residues for N binding. In the 11-mer peptide series, phosphomimetic substitutions increased the affinity of F_{11}, 9-fold for F_{11SE} and 20-fold for F_{11EE} (Figure 5B, Table 1). A closer inspection of the binding curves shows that F_{11SE} and F_{11EE} seem to display a second binding mode of weak affinity, which becomes visible once the canonical binding site has been saturated. For F_{11SE} this mode could be fitted with a linear contribution (Figure 5B, Table 1).

To validate fluorescent peptide binding to N-RNA, we carried out competition experiments with unlabeled P peptides. We used 10 μM of N protein. We first probed competition of the F_{11} peptide by three P peptides of different lengths: P_{7E}, P_{9E} and P_{11EE} (Figure 5C). These phosphomimetic peptides were able to fully displace F_{11}, with IC_{50} values ranging from 22 μM for the longest P_{11EE} peptide to 180 μM for the shortest P_{7E} peptide (Table 2). The trend of IC_{50} suggests that the efficiency of P peptides in competing with F_{11} increases with peptide length. This is in line with the increase of affinity observed with increasing length of fluorescent P peptides (Table 2). Inhibition constants, calculated with K_d values determined for F_{11}, ranged from 6 to 75 μM (Table 2). The trend of K_i was the same as that of IC_{50}. It is noteworthy that K_is of unlabeled peptides were higher than the K_ds of their FITC-labeled counterparts, suggesting that the fluorescent peptides may display higher affinities than the unlabeled ones.

Table 2. Inhibition parameters obtained by FP for FTU-labeled RSV P peptides (F_n) in complex with RSV N-RNA. Samples were in Tris pH 8 buffer without salt. IC_{50} values were determined from inhibition experiments with 10 μM N-RNA and 200 nM fluorescent probe. Fitting of the inhibition data was done with a Hill equation. K_i was calculated from IC_{50} and K_d using the IC50-to-Ki server [49].

F_n Peptide	Inhibitor	IC_{50} (μM)	K_i (μM)	K_d of F_n Peptide (μM) *	K_d of F_n Equivalent to Inhibitor (μM) *
F_{11}	P_{11EE}	22 ± 4	6	7.6	0.38/0.15
F_{11}	P_{9E}	66 ± 6	25	7.6	2.2
F_{11}	P_{7E}	180 ± 11	75	7.6	2.5
F_{11}	P_{11}	86 ± 7	34	7.6	7.6
F_{7E}	P_{7E}	376 ± 26	74	2.5	2.5
F_{5E}	P_{5E}	433 ± 21	158	5.9	5.9
F_{11}	M76	13 ± 2	3	7.6	
F_{7E}	M76	48 ± 5	8	2.5	

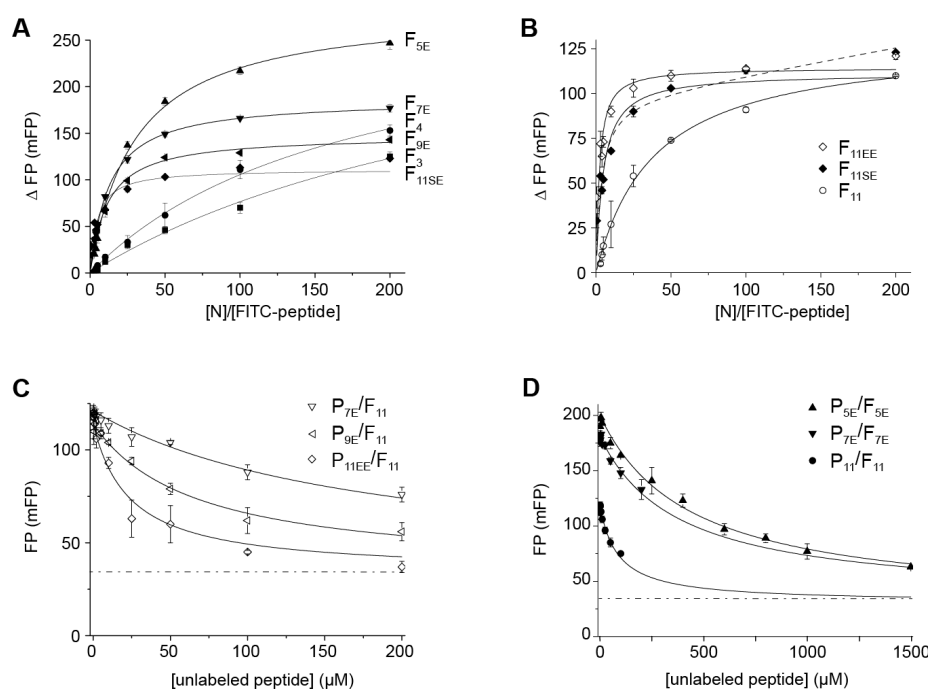* K_d values of F_n peptides are from Table 1.

Figure 5. Binding of FTU-labeled RSV P peptides (F_n) to RSV N-RNA and inhibition by unlabeled peptides assayed by FP. Data were acquired after 30 min incubation. Samples were in Tris pH 8 buffer without salt. The concentration of fluorescent probes was 200 nM. (**A**) Binding of N-RNA to F_n peptides was assayed by ΔFP as a function of the N:peptide molar ratio for peptides of various lengths. FP of free fluorescent peptide was FP_{min} ~30–40 mFP. Error bars represent the standard deviation of triplicate measurements. Curves were fitted with a single binding site model. (**B**) ΔFP binding curves for 11-mer fluorescent peptides (wild-type F_{11}, Ser$_{237}$Glu mutant F_{11SE} and double Ser$_{232}$Glu/Ser$_{237}$Glu mutant F_{11EE}) with N-RNA. Data were fitted with a single binding site model (straight lines). For F_{11SE} a second calculated curve in broken line corresponds to a model with an additional linear component. (**C**) Inhibition curves of N-RNA (10 µM) binding to F_{11} by the unlabeled P_{7E}, P_{9E} and P_{11EE} peptides. Data were fitted with a Hill equation. The dashed line indicates the mean FP value of free F_{11}. (**D**) Inhibition curves of N-RNA (10 µM) binding to F_n peptides by unlabeled P peptides containing the same amino acid composition.

We next made competition experiments between three fluorescent and unlabeled peptides with identical amino acid sequences: F_{5E} vs. P_{5E}, F_{7E} vs. P_{7E} and F_{11} vs. P_{11} (Figure 5D, Table 2). The unlabeled peptides were able to fully displace their fluorescent counterparts. IC_{50} and K_i values decreased with increasing peptide length, underlying the importance of P peptide length for inhibition of the N-P complex. Comparison of P_{11} with P_{11EE} for inhibition of F_{11} binding (Table 2) showed that P_{11} competed less efficiently than P_{11EE} with an IC_{50} of 86 versus 22 µM (K_i of 34 versus 6 µM). This confirms the role of additional negative charges for formation of the RSV N-P complex.

Finally, we probed inhibition by the M76 molecule of F_{11} and F_{7E} in complex with N-RNA. M76 IC_{50} and K_i values were in the µM range, but still lower than those of any tested unlabeled P peptide, indicating that M76 is a more potent inhibitor than the peptides, including P_{11EE}. Moreover, M76 appears to be more potent to inhibit the N-F_{11} complex than the N-F_{7E} complex (K_i of 2.6 versus 8 µM). Although F_{11} and F_{7E} cannot be directly compared because of their different lengths, this finding suggests that M76 is less efficient at competing with a phosphomimetic peptide. A rationale for this would be that M76 directly competes with Phe$_{241}$, but not with Ser/Glu$_{237}$ that binds outside of the cavity.

It must be noted that measurements with N_{NTD} and N-RNA were done at different pH. Fluorescein fluorescence depends on pH, since the phenols and carboxylic acid groups can be ionized in a pH-dependent manner [50]. At pH 6.5, fluorescein dianion and monoanion forms are in a 1:1 equilibrium, whereas at pH 8.0 the dianion is predominant [51]. At pH 6.5

fluorescence emission at 490 nm is thus decreased by 30–40% as compared to pH 8 [52]. Nevertheless, FP should not be affected by pH, since fluorescence polarization is a ratio of emitted fluorescence intensities (Equation (4)). However, lower fluorescence leads to a lower signal-over-noise ratio at pH 6.5. In conclusion, N-RNA in a pH 8.0 buffer appears to be better suited for an FP inhibition assay than N_{NTD} in a pH 6.5 buffer.

2.5. Fluorescein Binds to the RSV P-Binding Site on RSV N Protein

Although unlabeled P peptides were able to displace their fluorescent counterparts from RSV N-RNA, we wondered if the difference between the K_i of F_n peptides and the K_d of unlabeled peptides could originate in N-RNA binding of the fluorescein label. We therefore measured fluorescein FP in the presence of N-RNA. We obtained a binding curve (Figure 6B). Complete saturation of fluorescein by N-RNA was not reached in the N concentration range used for the experiment. We tentatively extracted a K_d of 91 µM (Table 3) from these binding data, assuming that FP_{max} reaches the maximal theoretical value (500 mFP). The binding affinity was lower than that measured for F_n peptides, but still significant. The contribution of fluorescein binding to FP could be non-negligible, especially for the shorter F_3 and F_4 peptides, for which we determined K_ds of 62 and 35 µM, respectively (Table 1). However, the affinity of fluorescein was lower by at least of one order of magnitude as compared to peptides longer than F_{5E}. Hence, for these peptides, the fluorescent label is not expected to strongly compete with the peptide part. To test if fluorescein binds to the P-binding site on the N-RNA, we carried out a competition experiment with M76 (Figure 6C). M76 was able to displace fluorescein rather efficiently, with an IC_{50} of 27 µM and a K_i of 13 µM (Table 3), indicating that fluorescein indeed targets the P-binding site of the N protein.
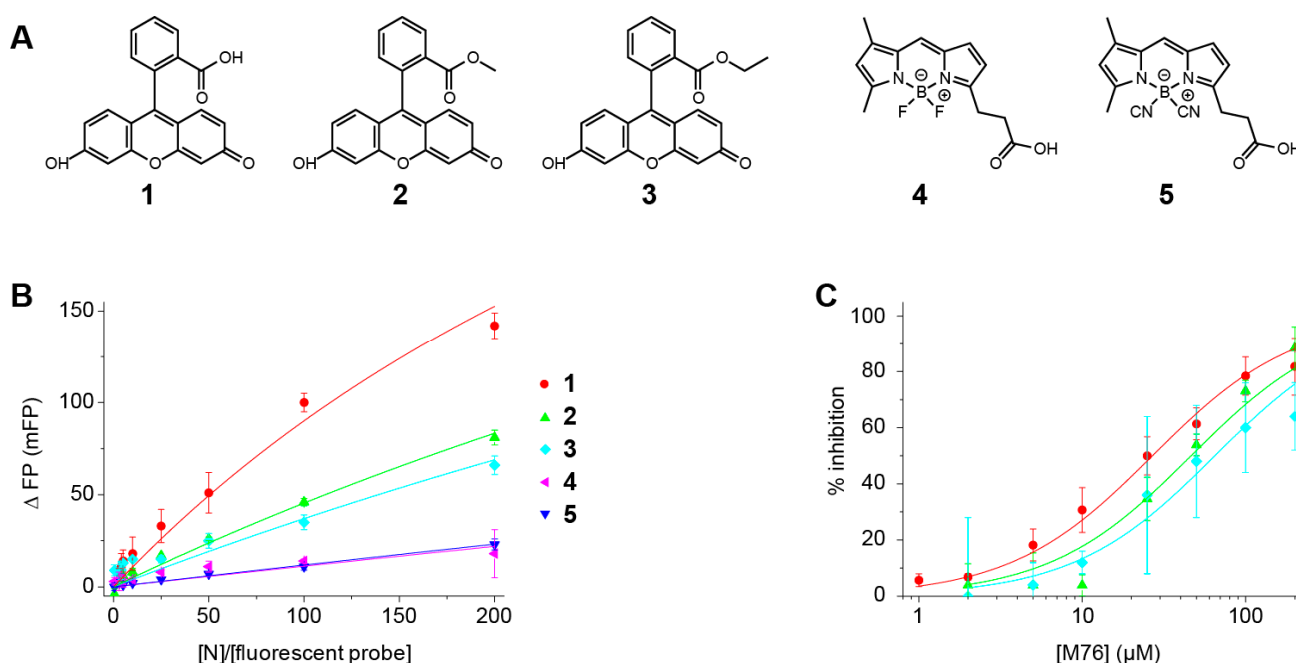

Figure 6. Binding of fluorescent molecules to RSV N-RNA and inhibition by M76 assayed by fluorescence polarization. Measurements were carried out in Tris pH 8, Brij-35 buffer without salt. The concentration of fluorescent probes was 200 nM. (**A**) Chemical structure and name of fluorescent molecules. For fluorescein **1**, the open form is shown. Fluorescein methyl ester **2**; fluorescein ethyl ester **3**; 4,4′ difluoro BODIPY FL **4**; 4,4′ dicyano BODIPY FL **5**. (**B**) ΔFP binding curves of fluorescent molecules as a function of the N:fluorescent molecule molar ratio. Fits were performed assuming FP_{max} = 500 mFP and FP_{min} = 0 mFP. (**C**) Inhibition of fluorescent molecule binding to N-RNA (20 µM) by M76.

Table 3. Parameters for binding to RSV N-RNA and inhibition by M76 obtained for fluorescent molecules from FP. Apparent K_ds were calculated assuming FP_{max} = 500 mFP. IC_{50}s were determined from inhibition experiments with 20 μM N-RNA and 200 nM fluorescent probe. K_is were calculated from IC_{50} and K_d using the IC50-to-Ki server [49].

Fluorescent Molecule	K_d (μM)	M76 IC_{50} (μM)	M76 K_i (μM)
Fluorescein 1	91 ± 5	27 ± 2	13
Fluorescein methyl ester 2	200 ± 8	46 ± 7	32
Fluorescein ethyl ester 3	250 ± 27	65 ± 9	50
4,4′ difluoro BODIPY FL 4	870 ± 140	(*)	(*)

(*) not determined.

To validate binding of fluorescein to the P-binding site, we made an NMR titration experiment with ^{15}N-labeled N_{NTD}, using experimental conditions similar to those of the titration of N_{NTD} by the pP_{11} peptide. Fluorescein induced CSPs located in the same region as those induced by pP_{11} (Figure 7A), indicating that fluorescein targets the P-binding site of N_{NTD} (Figure 7B,C). To get atomic details about the N_{NTD}-fluorescein complex, we run docking experiments using 2 docking softwares: MOE with GBVI/WSA dG scoring function [53] and SMINA with Vinardo scoring function [54]. Two different poses of fluorescein inserted into the P-binding pocket were predicted (Figure 7D). Fluorescein was modeled in its open, fluorescent form. In all cases, one of the xanthene rings was inserted into the hydrophobic P-binding pocket of N_{NTD}, and the benzoic acid was positioned similarly to the pyrazole ring of M76, forming salt bridges with R150 or R132 (Figure 7D,E).

To avoid interference of the fluorophore with FP measurements, we sought to lower the affinity of fluorescein for RSV N protein, while retaining fluorescence property, by chemical modifications. We produced methyl and ethyl esters of the benzoic acid to change the charge and the size of the molecule (Figure 6A). A series of FP measurements was made with different N-RNA concentrations. The two fluorescein derivatives also bound to N-RNA, but displayed 2-fold lower affinity (Figure 6B, Table 3). M76 was able to displace these two variants (Figure 6C). K_is were of the same order of magnitude at the K_i of fluorescein (Table 3). These binding and inhibition experiments suggest that the behavior of the two fluorescein derivatives is close that of the original molecule. Indeed, fluorescein methyl ester adopted docking poses similar to those of fluorescein.

2.6. An FP Assay for the RSV N-P Interaction Using Full-Length N and BODIPY FL-Labeled P Peptides

The undesirable binding of fluorescein to N-RNA led us to reconsider the BODIPY FL as label for peptides, despite the preliminary mixed results obtained with this fluorophore. To get rid of the instability problems encountered with 4,4′ difluoro BODIPY FL scaffold, we considered its 4,4′ dicyano analogue reported as being more stable and with better photo-physical properties. Such derivatives were recently described as tags for bioconjugation [55,56], but, to our knowledge, not for an FP assay. While difluoro-**4** and dicyano BODIPY FL **5** also bound to N-RNA, FP values were markedly lower than those of fluorescein at the same N-RNA concentrations (Figure 6B), suggesting that BODIPY FL is less prone to bind. The K_d for **4**, obtained by fitting the ΔFP data with FP_{max} = 500 mFP, was also higher than that of fluorescein (Table 3). Altogether, these results show that the nature of the fluorophore must be taken into account in an FP assay with RSV N and P proteins, and that BODIPY FL is less prone than fluorescein to affect FP measurements. Moreover, as compared to difluoro BODIPY FL-labeled peptides, dicyano BODIPY FL-labeled peptides were chemically stable (either under the acidic conditions used for their purification by HPLC or under the conditions of the FP assay). To assess the properties of BODIPY FL as a fluorescent label for P peptides, we produced a new series of eight dicyano BODIPY FL-labeled (BCN_n) peptides of variable length (Table 4) and tested them for N-RNA binding.
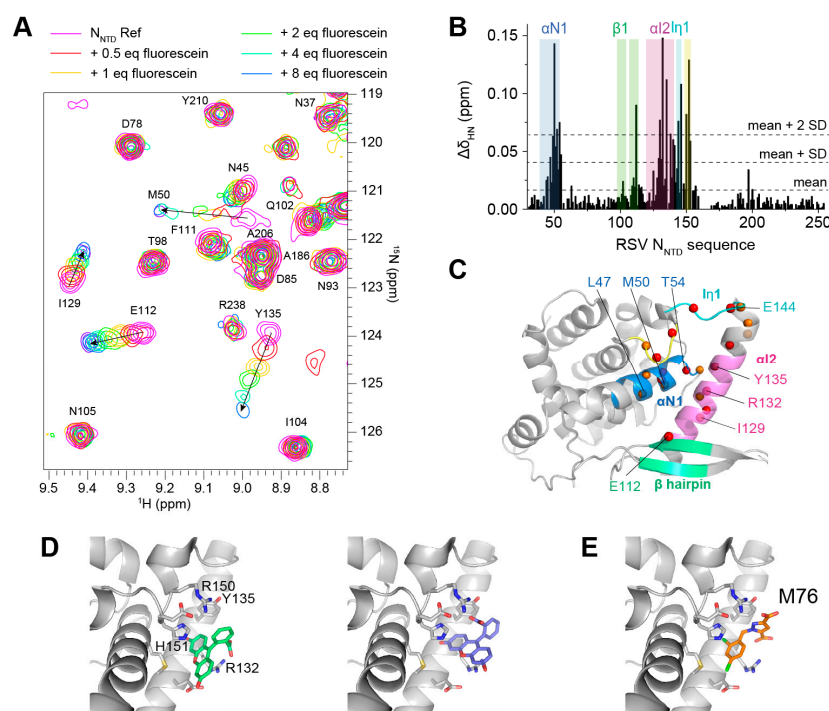
Figure 7. Analysis of fluorescein binding to RSV N_{NTD} by NMR and by in silico docking. (**A**) Selected region of superimposed ^{1}H-^{15}N HSQC spectra of ^{15}N-labeled RSV N_{NTD} obtained during titration by fluorescein. NMR data were acquired at a magnetic field of 14.1 T, a temperature of 20 °C, and with 50 μM ^{15}N-N_{NTD} concentration. The color code corresponds to the fluorescein:N_{NTD} molar ratio, as indicated on top. (**B**) Bar diagram of combined ^{1}H and ^{15}N amide chemical shift perturbations ($\Delta\delta_{HN}$) measured in the presence of 2 molar equivalents of fluorescein. (**C**) Mapping of CSPs onto the X-ray structure of N_{NTD} (PDB 4ucc). Amide nitrogens are represented as red and orange spheres for residues with $|\Delta\delta_{HN}| >$ mean + 2 SD and $|\Delta\delta_{HN}| >$ mean + SD, respectively. Regions with significant CSPs are labeled with the same color code on the structure and on the diagram in (**B**). (**D**) Two docking poses of fluorescein binding to N_{NTD}: the first pose was obtained with MOE (green) and the second with Smina (blue). (**E**) X-ray crystal structure of the N_{NTD}-M76 complex (PDB 4ucc).

Table 4. Dicyano BODIPY FL-labeled RSV P (BCN-P) peptides designed for FP measurements with RSV N-RNA and binding parameters obtained from FP. Samples were in Tris pH 8.0 buffer, without or with salt (100 mM NaCl). BCN_n peptide concentration was 200 nM. K_d and ΔFP_{max} were obtained by fitting binding curves to a single site binding model.

Fluorescent BCN_n Peptide	Fluorescent Peptide Sequence	ΔFP_{max} (mFP)	K_d (μM)	ΔFP_{max} (mFP)	K_d (μM)
		No Salt	No Salt	With Salt	With Salt
BCN_{11SE}	BCN-DSDNDLELEDF-OH	312 ± 25	0.82 ± 0.22	122 ± 2	0.55 ± 0.07
BCN_{11EE}	BCN-DEDNDLELEDF-OH	316 ± 12	0.28 ± 0.07	197 ± 5	0.26 ± 0.04
BCN_{10EE}	BCN-EDNDLELEDF-OH	270 ± 7	0.16 ± 0.03	171 ± 16	1.24 ± 0.31
BCN_{9E}	BCN-DNDLELEDF-OH	288 ± 15	0.96 ± 0.13		
BCN_{8E}	BCN-NDLELEDF-OH	298 ± 5	1.43 ± 0.08	284 ± 15 (*)	7.1 ± 0.1 (*)
BCN_{7E}	BCN-DLELEDF-OH	332 ± 8	2.2 ± 0.2		
BCN_{6E}	BCN-LELEDF-OH	275 ± 8	2.3 ± 0.2	281 ± 19 (*)	12.6 ± 1.6 (*)
BCN_{5E}	BCN-ELEDF-OH	431 ± 15	9.8 ± 0.9		

(*) Saturation of experimental binding curve not reached.

We first performed FP measurements in salt-free Tris pH 8 buffer (Figure 8A). We measured binding curves using 200 nM of fluorescent peptides. Measurements were stable within a time span of 1 h. Saturation by N-RNA was reached for all peptides, except for

the shortest one BCN_{5E}. Overall, the dynamic range of FP was more extended for BCN_n peptides than for F_n peptides, with ΔFP_{max} of 270–430 mFP, as compared to 95–315 mFP for F_n peptides (Table 4). Fitted K_ds were similar to those of their equivalent F_n peptides, suggesting that the fluorophore does not contribute to the affinity of P peptides longer than 5-mers. Overall, affinities increased with the length of the peptides. The BCN_n peptide series exhibited a similar trend to that of the F_n series, highlighting the binding contribution of residues beyond Asp_{240} and Phe_{241}. A gain of affinity was observed for BCN_{11EE} vs. BCN_{11SE}, showing that the phosphomimetic at position 232 contributes to binding.
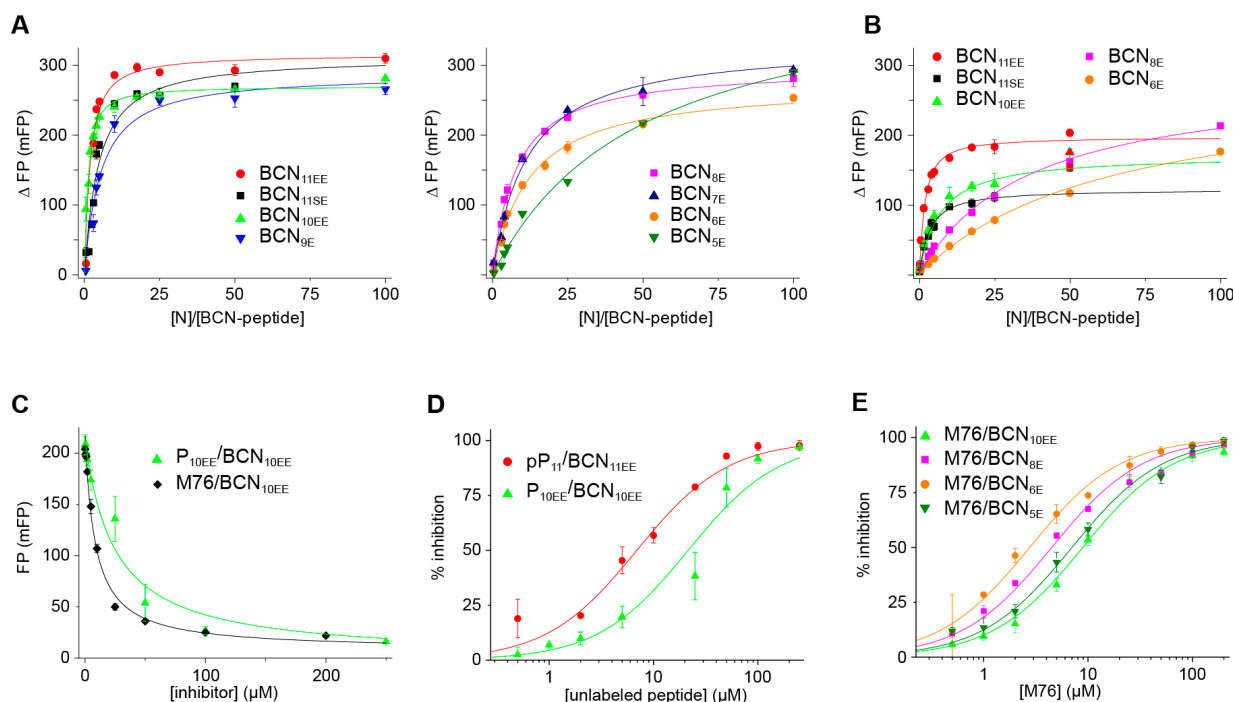

Figure 8. Binding of dicyano BODIPY FL-labeled C-terminal RSV P peptides to RSV N-RNA and inhibition assayed by FP. Samples were in Tris pH 8 buffer, with or without salt. The concentration of fluorescent peptides was 200 nM. Error bars represent the standard deviation of measurements in triplicate. Fitted curves are in straight lines. (**A**) ΔFP binding curves of fluorescent BCN_n peptides of various lengths to N-RNA in salt-free buffer ($FP_{min} \sim 10$ mFP). Data were fitted with a single binding site model. (**B**) ΔFP binding curves measured in buffer with salt (100 mM NaCl). (**C**) Inhibition of N-RNA (1 µM) binding to B_{10EE} peptide by unlabeled P_{10EE} peptide and by M76. Data were fitted with a Hill equation. (**D**) Inhibition of N-RNA (1 µM) binding to two BCN_n peptides (BCN_{10EE} and BCN_{11EE}) by unlabeled P peptides with equivalent amino acid sequences (P_{10EE} and pP_{11}). (**E**) Inhibition by M76 of N-RNA (2 µM) binding to fluorescent peptides BCN_{5E}, BCN_{6E}, BCN_{8E}, and BCN_{10EE}.

To evaluate the quality of FP measurements, we performed a Z' assay [57,58] with the BCN_{10EE} peptide. An N-RNA concentration of 1 µM afforded a high dynamic range ($\Delta FP_{max} = 220 \pm 13$ mFP, with $FP_{min} = 9 \pm 3$ mFP). We determined a Z' value of 0.78 from seven data points, which validates the BCN_{10EE} probe. We further tested robustness with respect to solvent. FP values were not significantly affected by addition of up to 5% ethanol and 10% DMSO.

As compared to salt-free buffer, the ΔFP_{max} range in salty buffer (100 mM NaCl) was significantly reduced for the long BCN_{10EE}, BCN_{11SE} and BCN_{11EE} peptides (Figure 8B, Table 4). This is similar to what was observed for the F_{11} peptide. The fluorescent label of long P peptides thus appears to be more mobile under salty conditions, likely due to screening of electrostatic interactions involving acidic amino acids of P peptides. This was not observed for the shorter B_{6E} and B_{8E} peptides. However, it must be noted that

the binding curves of BCN_{6E} and BCN_{8E} did not reach a plateau within the N-RNA concentration range used in our FP experiments, which may affect the fitted parameters. The affinity of BCN_{6E} and BCN_{8E} peptides decreased 5-fold in salty buffer, and that of BCN_{10EE} 8-fold, as expected by screening of electrostatic interactions in a higher ionic strength buffer. Intriguingly, similar affinities were measured for BCN_{11EE} and BCN_{11SE} under both salt conditions, despite the phosphomimetic substitution in BCN_{11EE}.

To further investigate the complex between BCN_n peptides and N-RNA, we made competition experiments between unlabeled peptides and fluorescent peptides of same length and/or charge, using the P_{10EE}/BCN_{10EE} and pP_{11}/BCN_{11EE} pairs. The unlabeled peptides were able to fully displace their fluorescent equivalents (Figure 8C), and the inhibition curves could be fitted with a Hill equation (Figure 8D). The K_is of unlabeled peptides were in the μM range (Table 5).

Table 5. Inhibition parameters obtained by FP for dicyano BODIPY FL-labeled RSV P peptides in complex with RSV N-RNA. Samples were in Tris pH 8 buffer. Fluorescent probe concentration was 200 nM. N concentration was between 1 and 20 μM as indicated. IC_{50} and FP_{max} were obtained by fitting the inhibition data with a Hill equation. K_i was calculated using the IC50-to-Ki server [49].

Fluorescent Peptide	Inhibitor	[N−RNA] (μM)	Fitted FP_{max} (mFP)	Fitted IC_{50} (μM)	K_i (μM)	K_d (μM) of BCN-P Peptide (*)
BCN_{10EE}	P_{10EE}	1	214	21 ± 4	2.9	0.16
BCN_{11EE}	pP_{11}	1	234	6.9 ± 1.2	1.4	0.28
BCN_{11SE}	M76	5	280	17 ± 2	1.8	0.8
BCN_{10EE}	M76	2	257	8.9 ± 0.6	0.5	0.16
BCN_{10EE}	M76	1	219	8.5 ± 0.6	1.1	0.16
BCN_{8E}	M76	5	196	13 ± 2	2.0	1.4
BCN_{8E}	M76	2	166	4.5 ± 0.4	1.3	1.4
BCN_{6E}	M76	10	177	14 ± 1	1.1	2.3
BCN_{6E}	M76	2	104	2.7 ± 0.2	0.7	2.3
BCN_{5E}	M76	20	280	26 ± 2	3.6	9.8
BCN_{5E}	M76	2	76	7.0 ± 0.6	4.8	9.8

(*) K_ds of the BCN_n peptides are from Table 4.

To probe the potency of M76 as an inhibitor, we carried out competition experiments with the M76 molecule and several BCN_n peptides. M76 was able to displace the fluorescent probes from N-RNA, and inhibition curves were obtained (Figure 8E). Since we used different N concentrations to have similar dynamic ranges of FP for the series of fluorescent peptides, we cannot directly compare M76 IC_{50}s. However, K_is may be compared. K_i values were of the same order of magnitude, 0.5–1.8 μM, for peptides longer than B_{6E} (Table 5), suggesting that the inhibition mechanism by M76 is the same for these BCN_n peptides. Inhibition of BCN_{5E} yielded slightly higher K_i values (3.6–4.8 μM), but the K_d determined from a non-saturating binding curve might bias the result. M76 appeared to be more potent than the P_{10EE} peptide to displace BCN_{10EE} from N-RNA with a K_i of 1.1 versus 2.9 μM (Table 5).

3. Discussion

Recognition of the RSV nucleocapsid by the RNA polymerase proceeds via a specific interaction between the essential RSV phosphoprotein polymerase cofactor P and the RSV nucleoprotein N in complex with genomic RNA. This interaction relies on the most C-terminal residue of P, Phe_{241}, which inserts into a pocket at the surface of N. This view is supported by X-ray crystal structures of phenylalanine or short C-terminal P peptides in complex with the RSV N_{NTD} construct, revealing the Phe_{241} aromatic moiety as a main structural element that drives P binding thanks to well-defined interactions with N atoms delineating a binding pocket. Recently, Phe_{241} was further confirmed to be the main determinant for P anchoring to N by in silico energetic analysis and mutational analysis of Phe_{241} in vitro [59]. This view is also supported by in vitro binding and polymerase

activity assays. While the aromatic $Phe_{241}Trp$ substitution maintained N binding, deletion of Phe_{241} and substitution of Phe_{241} by smaller amino acids like alanine and aspartate impaired N binding [31]. In vitro polymerase activity, as assessed with a minigenome, was completely abrogated by the $Phe_{241}Ala$ mutation [21]. However, even though Phe_{241} acts as a linchpin, adjacent residues also significantly contribute to the RSV N-P complex. The $Leu_{238}Ala$ and the double $Glu_{239}Ala/Asp_{240}Ala$ mutants reduced minigenome activity 2-fold [21]. Early investigations led to the conclusion that a tract of nine C-terminal residues was necessary and sufficient for N binding [31]. Later we showed that a 12-mer peptide displayed approximately the same affinity in vitro as the full P_{CTD} domain, with K_d of 30–55 µM in salty buffer [33]. Affinity is expected to be rather weak, due to the requirement for polymerase processivity to elongate the newly synthesized RNA. Structural analysis of the RSV phosphoprotein by solution NMR indicated that P_{Ctail} remained unstructured in solution in the context of full-length P [26]. In contrast to other linear protein-binding motifs in P, like the binding sites for N^0, M2-1 or L proteins, that transiently fold into α-helices and are stabilized in complex, P_{Ctail} did not display any propensity for any secondary structure, neither α-helical nor extended [29]. This is a strong indication that P_{Ctail} does not adopt any secondary structure in complex with N protein either. This implies that the entropic cost of binding likely remains moderate and that nearly all C-terminal amino acids of P may individually contribute to strengthen the N-P complex, even if they do not adopt a defined position.

The amino acid sequence of RSV N protein is rather conserved, and thus of particular interest for drug design [60,61]. The RSV N protein had already been identified before as a target for post-entry inhibitors. Notably the benzodiazepine RSV604, which reached phase II clinical trial before being discontinued, was proposed to bind to the N protein, since it elicited escape mutants on N [62,63]. Recently, EDP-938, another benzodiazepine in phase 2a clinical trial, was reported to target RSV N, also eliciting several mutations on N close to the P-binding pocket [42] leading to resistance. Based on the inhibitory potential of the M76 molecule we have suggested that the RSV P-binding pocket on N might be druggable [33]. This hypothesis was based on the assumption that a suitable inhibitor would be a direct competitor of the $Asp_{240}Phe_{241}$ dipeptide. If the interaction surface of the N-P complex extends beyond the $Asp_{240}Phe_{241}$ binding site and if up to 10 residues away from Phe_{241} contribute to the interaction energy, this raises the question if targeting the P-binding site with a small molecule would be sufficient to inhibit the N-P complex and displace P_{Ctail} and full-length P. In turn, this raises the question about how to design a meaningful assay to screen for inhibitors of the RSV N-P interaction. To address this question we sought for a more comprehensive view of the fuzzy complex formed between RSV N and C-terminal peptides to propose a relevant model of this interaction.

An inhibition assay by fluorescence polarization relies on the size difference between a free fluorescent probe and its complex with a target protein. We tested two forms of the nucleoprotein, the N_{NTD} domain and the N-RNA complex. Our results suggest that the N_{NTD} domain, although suitable in terms of size, induces binding biases, in particular one or more secondary interaction sites and binding of fluorescent labels to the P-binding pocket. In the N-RNA complex, which is structurally close to the nucleocapsid, the N protein surface is not fully accessible, which reduces unspecific binding, and even the P-binding site appears to be rather occluded (Figure 1B,C). N-RNA thus appears to be more relevant than N_{NTD} and the monomeric RNA-free N^0-like N mutant used by Shapiro et al. [45]. Interestingly, Shapiro et al. had suggested a difference in binding affinity between BODIPY FL-labeled and unlabeled P_{11} by comparing FP and SPR data, which hints at binding of the fluorescent label [45]. Here, we show that binding of BODIPY FL remains moderate as compared to fluorescein, and that the peptide part of BCN_n peptides longer than 5-mers provides the main driving force for N-RNA binding. Steric hindrance in the N-RNA complex context could thus act as a filter to discriminate between specific and unspecific N binding.

Since C-terminal RSV P-peptides are highly negatively charged, electrostatic interactions likely play an important role for the affinity of the RSV N-P complex. We confirmed the role of electrostatic interactions by comparing binding affinities for several fluorescent P peptides in salty versus salt-free buffers. In salt-free buffer, sub-micromolar affinity could be achieved. This is an asset for an FP assay to eliminate low binding molecules and rank high-affinity inhibitors in an HTS inhibition assay. Shapiro et al. reported a 20-fold increase in affinity by phosphorylation of Ser_{232} and Ser_{237} residues in the P_{11} peptide [45]. We observed similar effect on affinity by using phosphomimetic peptides, which exacerbate electrostatic interactions with N.

We previously assessed that the N-P complex was fuzzy, with the C-terminal Phe_{241} serving as a main anchor. To illustrate the dynamics at the P-binding site, we built a 3D structural model of the N_{NTD}-P_{11} complex by docking the P_{11} peptide onto N_{NTD}, using the Haddock webserver (Figure 9A–C). For this purpose, we used a structure of N_{NTD} extracted from the N_{NTD}-P_2 complex X-ray structure (PDB 4uc9) and generated structural models of P_{11} using the PEP-FOLD3 server [64]. The structural ensemble of free P_{11} was highly disordered, with the exception of the C-terminus that displays an incomplete α-helical turn involving residues Glu_{239}-Phe_{241} (Figure 9D). The 9 N-terminal residues of P_{11} (Asp_{231}-Glu_{239}) were allowed to remain flexible during docking. Docked P_{11} also displayed a high degree of disorder, and the α-helical turn partly unwound (Figure 9C). Overall, docked P_{11} structural models were more extended than free P_{11} models, but it cannot be excluded that this is due to the difference of algorithms implemented in Haddock and PEP-FOLD3.
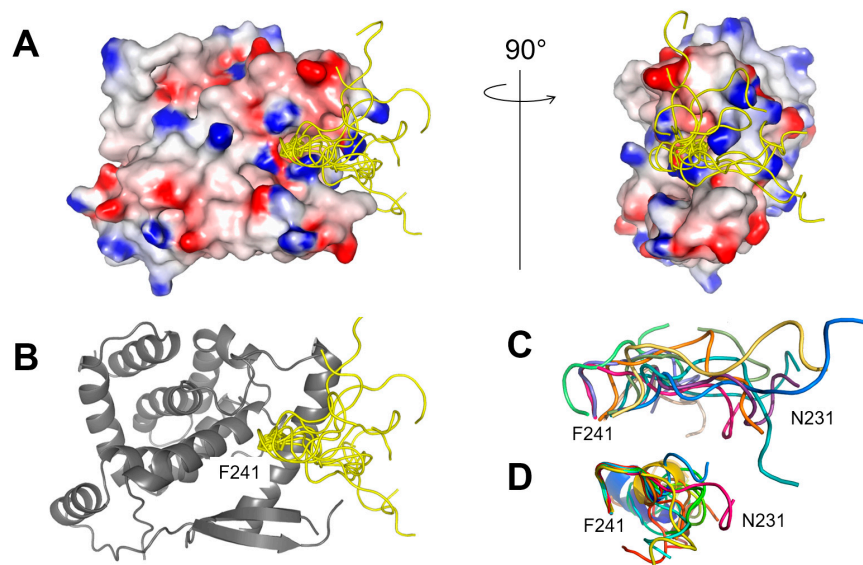

Figure 9. Structural model of the RSV N_{NTD}-P_{11} complex. (**A**,**B**) Structures were generated with Haddock software [65], based on the crystal structure of the N_{NTD}-P_2 complex (PDB 4uc9) for N_{NTD} and on a P_{11} model generated with PEP-FOLD3 [64]. 10 models were superimposed. The docked P_{11} peptides are in yellow cartoon. (**A**) Two views of N_{NTD} rotated by 90° show the electrostatic surface potential calculated with Delphi software [66], with a scale ranging from −10 (red) to +10 kcal.mol^{-1} (blue). (**B**) The backbone of N_{NTD} is shown in cartoon representation. (**C**) The P_{11} starting structure used for Haddock docking, in magenta, was aligned with the docked structures represented in other colors. The view is rotated, as compared to (**A**,**B**). (**D**) 20 P_{11} models generated with PEP-FOLD3 were structurally aligned along the three C-terminal residues Glu_{239}-Phe_{241}. The model used for Haddock docking is in magenta, and the other models in colors unrelated to those used in (**C**).

The electrostatic surface potential of N_{NTD} does not reveal a unique positively charged surface area, but rather a number of anchoring points afforded by positively charged residues. P_{11} displays neither defined conformation nor position, but seems to adopt a preferential orientation towards a positively charged patch located near the exit the cavity occupied by Phe_{241} (Figure 9A). This structural model provides a rationale for the overall

increase of binding affinity observed with increasing peptide length up to 11 amino acids. Each amino acid contributes to binding affinity, either by electrostatic or van der Waals interactions. It also explains the concomitant decrease of FP in fluorescently labeled P peptides. As the label is attached to the opposite N-terminal side of the peptide, the fluorescent label experiences increased motional freedom, when the length of the tether increases. As the majority of C-terminal P peptide residues is charged, it is not surprising that a decrease in FP is observed in buffers with higher ionic strength.

As compared to difluoro BODIPY FL-labeled peptides, dicyano BODIPY FL-labeled peptides were more stable. The FP dynamic range was more extended for BCN_n peptides than for F_n peptides: This is an advantage for an FP assay. An FP assay relies on a compromise between peptide length and mobility of the fluorescent label. In this respect, 10-mer or 11-mer BCN_n peptides, which bind with sub-micromolar affinity in salt-free buffer and offer an extended dynamic FP range, appear to be suitable. Finally, M76 proved to be a suitable benchmark to screen for inhibitors, as it is able to fully displace even longer fluorescent P peptides.
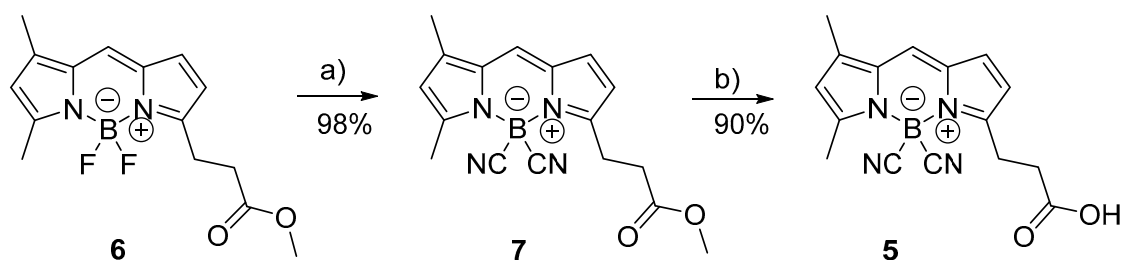
4. Materials and Methods

4.1. Materials

All commercially available reagents and solvents were used as received unless otherwise noted. Fluorescein and fluorescein sodium salt were purchased from Sigma-Aldrich. Fluorescein-5-isothiocyanate (FITC) and all other reagent used for peptide synthesis were purchased from Fluorochem (Hadfield, UK) and Iris Biotech GmbH (Marktredwitz, Germany). pP_{11} and P_{11SS} peptides (>95% purity assessed by HPLC) were purchased from GeneCust (Luxemburg). 1-(2,4-dichlorobenzyl)-1H-pyrazole-3,5-dicarboxylic acid (M76) was purchased from ChemBridge. 2-Chlorotritylchloride resin (theoretical loading of 1.6 mmol/g) was obtained from Merck (Molsheim, France). Flash chromatography purifications were performed using the automated chromatography Reveleris® Flash System (Grace, Büchi, Villebon-sur-Yvette, France) using prepacked normal phase cartridges from Interchim. Purifications were tracked with a dual λ absorbance UV detector and an ELSD detector.

HPLC analyses were performed on Hypersil C18 column (120 Å, 5 μm, 150 × 4.6 mm) using Waters Alliance 2690 separation module equipped with a Single Quadrupole Detector 2 (ESI quadrupole mass spectrometer), an ELS detector (Waters 2420) and a photodiode array detector (Waters 996). Reversed-phase ultra performance liquid chromatography-mass spectrometry (RP-UPLC-MS) analyses were performed on Waters equipment consisting of an ACQUITY UPLC H-Class separation module, photodiode array detector (eLambda detector), and a ESI triple quadrupole mass spectrometer (TQ detector). The analytical column used was the ACQUITY UPLC BEH C18 column (130 Å, 1.7 μm, 2.1 mm × 50 mm) operating at 0.6 mL·min^{-1} with linear gradient programs in 2.5 min run time (classical program: 5 to 100% of B in 2.5 min). UV monitoring was performed most of the time between 200 and 500 nm and was extracted at 214 nm. Solvent A consisted of H_2O containing 0.1% (*v*/*v*) formic acid and solvent B was CH_3CN containing 0.1% (*v*/*v*) FA. RP-HPLC purifications were performed on Waters equipment consisting of a 2545 quaternary pump, a photodiode array detector (Waters 2998), and an injector collector (Waters 2767). The preparative column, XBridge BEH C18 column (130 Å, 5 μm, 30 mm × 150 mm) was operated at 30 mL·min^{-1} with linear gradient programs in 15 min run time. The semi-preparative column, XBridge BEH C18 column (130 Å, 5 μm, 10 mm × 150 mm) was operated at 5 mL·min^{-1} with linear gradient programs in 15 min run time. Solvent C consisted of H_2O containing 0.1% (*v*/*v*) TFA and solvent D consisted of CH_3CN containing 9.9% (*v*/*v*) H_2O and 0.1% TFA. Classical focused programs on preparative or semi-preparative column: 10 or 20% (*v*/*v*) slope of D in 15 min. Water was of Milli-Q quality and was obtained after filtration of distilled water through a Milli-Q cartridge system. CH_3CN, FA, and TFA were of spectroscopic grade. High resolution mass spectra (HRMS-ESI) were obtained on a LCT Waters XE mass spectrometer equipped with an electrospray ionisation source. NMR spectra were performed on Bruker Avance spectrometers operating at 699 MHz for ^1H

NMR, 176 MHz for ^{13}C NMR, 282 MHz for ^{19}F and 160 MHz for ^{11}B NMR experiments. The chemical shifts are reported in ppm relative to tetramethylsilane with the solvent resonance as the internal standard. Multiplicities were given as: s (singlet); d (doublets); t (triplets); q (quadruplets) m (multiplets). Coupling constants are reported as a J value in Hz.

4.2. Synthesis of Fluorescent Molecules

The fluorescein methyl ester **2** and ethyl ester **3** were synthetized in 73% and 40% yield from fluorescein according to Lu et al. [67] and C. Y. Ng et al. [68], respectively. Difluoro BODIPY FL **4** was synthesized according to Gießler et al. [69]. The dicyano BODIPY FL **5** was synthesized in two steps from the difluoro BODIPY FL methyl ester (Scheme 1). The latter was obtained according to K. Gießler et al. [69].

Scheme 1. Synthesis of dicyano BODIPY FL **5**. (**a**) BF$_3$.OEt$_2$, TMSCN, DCM, 2 h; (**b**) THF/H$_2$O/HCl conc, 12 h.

Synthesis of methyl 3-(5,5-dicyano-7,9-dimethyl-5H-4λ^4,5λ^4-dipyrrolo [1,2-*c*:2′,1′-*f*] diazaborinin-3-yl)propanoate (**7**): BF$_3$·OEt$_2$ (34.0 μL, 0.27 mmol) was added to a cooled solution of difluoro BODIPY FL derivative **6** (415 mg, 1.36 mmol) in anhydrous CH$_2$Cl$_2$ (70 mL) at 0 °C. The mixture was then stirred at 25 °C for 10 min and TMSCN (851 μL, 6.80 mmol) was added. The reaction mixture was stirred at room temperature for 2 h. A saturated aqueous NaHCO$_3$ solution was added. The organic phase was washed with water and was dried over Na$_2$SO$_4$. The solvent was evaporated under reduced pressure to give the titled product as a red solid (0.43 g, 98%). ^{1}H NMR (699 MHz, CDCl$_3$) δ 7.22 (s, 1H), 7.06 (d, *J* = 4.30 Hz, 1H), 6.43 (d, *J* = 4.30 Hz, 1H), 6.31 (s, 1H), 3.73 (s, 3H), 3.45 (t, *J* = 7.20 Hz, 2H), 2.88 (t, *J* = 7.30 Hz, 2H), 2.74 (s, 3H), 2.31 (s, 3H); ^{13}C NMR (176 MHz, CDCl$_3$) δ 172.5, 161.2, 158.1, 145.3, 133.6, 131.7, 129.7, 126.02 (q, *J*$_{CB}$ = 75.2 Hz, 2 CN), 124.9, 122.1, 117.8, 52.3, 32.3, 24.3, 16.01, 11.7; ^{11}B NMR (160 MHz, CD$_2$Cl$_2$) δ −16.86 (s); ^{19}F NMR (282 MHz, CDCl$_3$) no peaks observed. HRMS [ESI]: *m/z* calculated for C$_{17}$H$_{17}$BN$_4$O$_2$ [M − H]$^-$ 319.1372; found: 319.1372.

Synthesis of 3-(5,5-dicyano-7,9-dimethyl-5H-4λ^4,5λ^4-dipyrrolo[1,2-c:2′,1′-f][1,3,2] diazaborinin-3-yl)propanoic acid (**5**): Concentrated HCl (16 mL) was added to a solution of methyl ester **7** (0.20 g, 0.62 mmol) in a mixture of THF (40 mL) and water (28 mL). The solution was stirred for 12 h at room temperature. Water (50 mL) and CH$_2$CL$_2$ (50 mL) were then added. The aqueous phase was extracted with CH$_2$Cl$_2$ (3 × 50 mL) and the combined organic phases were washed with brine and were dried over Na$_2$SO$_4$. The solvent was evaporated under reduced pressure to give the titled product as a red solid (0.17 g, 90%). M.p.: 211–232 °C. ^{1}H NMR (500 MHz, DMSO-*d*$_6$) δ 12.43 (s, 1H), 7.99 (s, 1H), 7.34 (d, *J* = 4.30 Hz, 1H), 6.63 (d, *J* = 4.20 Hz, 1H), 6.58 (s, 1H), 3.20 (t, *J* = 7.50 Hz, 2H), 2.82 (t, *J* = 7.50 Hz, 2H), 2.64 (s, 3H), 2.33 (s, 3H). ^{13}C NMR (176 MHz, DMSO-*d*$_6$) δ 173.1, 159.7, 157.5, 145.8, 132.8, 131.3, 130.3, 126.7, 125.5 (q, *J*$_{CB}$ = 74.0 Hz, 2CN), 121.9, 117.7, 31.2, 23.7, 15.1, 11.1. ^{11}B NMR (160 MHz, CD$_2$Cl$_2$) δ −17.0 (s). ^{19}F NMR (282 MHz, DMSO-*d*$_6$) no peaks observed. HRMS [ESI]: *m/z* calculated for C$_{16}$H$_{15}$BN$_4$O$_2$ [M − H]$^-$ 305,1288; found: 305.1198.

NMR spectra are given in Figures S1–S6. HPLC analysis of **5** and **7** is shown in Figures S31 and S32.

4.3. Peptide Synthesis

The BODIPY FL-labeled P peptide BF_2pP11 was synthesized from purchased pP_{11} peptide and BODIPY FL as described in [45].

P_3, P_4, P_{5E}, P_{5S}, P_{7S}, P_{7E}, P_{9E}, P_{9S}, P_{11SE} and P_{11EE} peptides and their fluorescent dicyano BODIPY FL conjugates BCN_{5E}, BCN_{6E}, BCN_{7E}, BCN_{8E}, BCN_{9E}, BCN_{10EE}, BCN_{11SE}, BCN_{11EE} were synthesized as described below.

Assemblies of protected peptides were carried out manually on 2-Chlorotritylchloride resin (theoretical loading of 1.6 mmol/g—0.2 g) using the Fmoc/*t*Bu strategy in a polypropylene reaction vessel fitted with polyethylene frits. After swelling of the resin for 15 min in CH_2Cl_2, the first amino acid was loaded through nucleophilic substitution by shaking the resin in a solution of Fmoc-Phe-OH (1 mmol/g) and DIPEA (1.5 equiv) in anhydrous CH_2Cl_2 (10 mL/g resin) for 30 min at room temperature. The un-reacted sites were then capped by shaking the resin in a mixture of MeOH/DIPEA/CH_2Cl_2 (2/1/17 *v/v/v*; 10.0 mL/g resin) for 10 min (repeated two times). The resin was then washed two times with DMF and three times with CH_2Cl_2 (10.0 mL/g resin) for 30 s. The overall process yielded a resin loading of around 0.65 mmol/g [determined from the dosage of the Fmoc released under the conditions of procedure A]. The number of reagent equivalents used in the following procedures is calculated from this resin loading. This step is followed by Fmoc removal according to procedure A. The elongation of the peptide was performed by cycle repetition of peptide coupling and Fmoc removal according to procedures B and A, respectively. Coupling of dicyano BODIPY FL, if required, was performed on the resin at the end of the peptide elongation on the amino terminus of the peptide according to procedure C. Cleavage of the peptide from the resin was carried out according to procedure D.

4.3.1. Procedure A: Fmoc Removal

N-α-Fmoc protecting groups were removed by shaking the resin in piperidine/DMF solution (1/4, *v/v*; 10.0 mL/g resin) for 5 min at room temperature. The process was repeated two times for 10 min, and the completeness of deprotection was monitored by ultraviolet absorption measurement of the filtrate at 299 nm. The resin was then washed five times with DMF and once with CH_2Cl_2 (10.0 mL/g resin) for 30 s.

4.3.2. Procedure B: Coupling Steps

Coupling reactions were performed by shaking with a solution of *N*-α-Fmoc-protected amino acid (2 equiv), PyBOP (2 equiv) and DIPEA (4 equiv) in DMF (10.0 mL/g resin) for 30 min at room temperature. The resin was then washed three times with DMF and once with CH_2Cl_2 (10.0 mL/g resin) for 30 s. Completeness of the coupling was controlled by TNBS and KAISER tests.

4.3.3. Procedure C: Coupling of Dicyano BODIPY FL

The resin was shaken with a solution of dicyano BODIPY FL **5** (1 equiv), DIPEA (4–8 equiv depending of the number of peptide acidic functions) and PyBOP (2 equiv) at room temperature in DMF (10.0 mL/g resin). The resin was then washed 14 times with DMF and 8 times with CH_2Cl_2 (10.0 mL/g resin) for 30 s.

4.3.4. Procedure D: Resin Cleavage and Protecting Groups Removal

The resin was first washed five times with CH_2Cl_2 (10.0 mL/g resin) before shaking in a mixture of TFA/TIS/H_2O MQ (95/2.5/2.5 *v/v/v*; 10.0 mL/g resin) for 2 h at room temperature and then filtrated. The resin was rinsed once with the same acidic mixture of TFA/TIS/H_2O MQ (95/2.5/2.5 *v/v/v*) for 1 min. The recovered solutions were concentrated under reduced pressure, and white solid was obtained by precipitation, triturating, and washing three times with diethyl ether. These crude peptides and crude dicyano BODIPY FL peptides, obtained as TFA salts, were purified by RP-HPLC on preparative or on semi-preparative column, respectively, using focused gradients, and freeze dried before their analysis by RP-UPLC-MS.

4.4. Peptide Purification and Yields

4.4.1. Unlabeled Peptides

UPLC traces and analysis for P_n peptides are given in Figures S7–S11.

- P_3 peptide was obtained as a white powder (34.0 mg, 50%). Analytical UPLC tr = 0.87 min; ESI-MS (positive mode) calculated for $[C_{18}H_{23}N_3O_8]$, 409.2; found m/z, 410.4 (M + H)$^+$. [Focused gradient 5–25% of B in 15 min].
- P_4 peptide was obtained as a white powder (49.0 mg, 59%). Analytical UPLC tr = 1.01 min; ESI-MS (positive mode) calculated for $[C_{24}H_{34}N_4O_9]$, 522.2; found m/z, 523.5 (M + H)$^+$. [Focused gradient 10–30% of B in 15 min].
- P_{5E} peptide was obtained as a white powder (59.0 mg, 59%). Analytical UPLC tr = 1.00 min; ESI-MS (positive mode) calculated for $[C_{29}H_{41}N_5O_{12}]$, 651.3; found m/z, 652.6 (M + H)$^+$. [Focused gradient 15–35% of B in 15 min].
- P_{7E} peptide was obtained as a white powder (43.0 mg, 33%). Analytical UPLC tr = 1.43 min; ESI-MS (positive mode) calculated for $[C_{39}H_{57}N_7O_{16}]$, 879.4; found m/z, 880.8 (M + H)$^+$. [Focused gradient 25–35% of B in 15 min].
- P_{9E} peptide was obtained as a white powder (27.0 mg, 17%). Analytical UPLC tr = 1.29 min; ESI-MS (positive mode) calculated for $[C_{47}H_{68}N_{10}O_{21}]$, 1108.5; found m/z, 1109.7 (M + H)$^+$. [Focused gradient 20–30% of B in 15 min].
- P_{11EE}: SPPS of P_{11EE} peptide was performed on 150 mg of 2-CTC resin. The peptide P_{11EE} was obtained as a white powder (28.0 mg, 20%). Analytical UPLC tr = 1.28 min; ESI-MS (positive mode) calculated for $[C_{56}H_{80}N_{12}O_{27}]$, 1352.5; found m/z, 1353.9 (M + H)$^+$. [Focused gradient 20–30% of B in 15 min].
- P_{11SE}: SPPS of P_{11SE} peptide was performed on 15.0 mg of 2-CTC resin. P_{11SE} was obtained as a white powder (4.50 mg) and was used without further purification for F_{11SE} synthesis.

4.4.2. Dicyano BODIPY FL-Labeled BCN_n Peptides

UPLC traces and analysis for BCN_n peptides and blank are given in Figures S21–S30.

- BCN_{5E}: Starting from P_{5E} on resin (8.71 µmol), BCN_{5E} was obtained as a red powder (2.63 mg, 32%). Analytical UPLC tr = 1.61 min; ESI-MS (negative mode) calculated for $[C_{45}H_{54}BN_9O_{13}]$, 939.8; found m/z, 939.4 (M − H)$^-$. [Focused gradient 38–48% of B in 15 min].
- BCN_{6E}: Starting from P_{6E} on resin (8.71 µmol), BCN_{6E} was obtained as a red powder (1.60 mg, 18%). Analytical UPLC tr = 1.74 min; ESI-MS (negative mode) calculated for $[C_{51}H_{65}BN_{10}O_{14}]$, 1052.5; found m/z, 1051.2 (M − H)$^-$. [Focused gradient 43–53% of B in 15 min].
- BCN_{7E}: Starting from P_{7E} on resin (8.71 µmol), BCN_{7E} was obtained as a red powder (2.22 mg, 22%). Analytical UPLC tr = 1.66 min; ESI-MS (negative mode) calculated for $[C_{55}H_{70}BN_{11}O_{17}]$, 1167.5; found m/z, 1166.9 (M − H)$^-$. [Focused gradient 40–50% of B in 15 min].
- BCN_{8E}: Starting from P_{8E} on resin (8.71 µmol), BCN_{8E} was obtained as a red powder (2.00 mg, 18%). Analytical UPLC tr = 1.56 min; ESI-MS (positive mode) calculated for $[C_{59}H_{76}BN_{13}O_{19}]$, 1282.6; found m/z, 1283.9 (M + H)$^+$. [Focused gradient 36–46% of B in 15 min].
- BCN_{9E}: Starting from P_{9E} on resin (8.71 µmol), B_{9E} was obtained as a red powder (1.17 mg, 10%). Analytical UPLC tr = 1.53 min; ESI-MS (positive mode) calculated for $[C_{63}H_{81}BN_{14}O_{22}]$, 1396.6; found m/z, 1398.2 (M + H)$^+$. [Focused gradient 35–45% of B in 15 min].
- BCN_{10EE}: Starting from P_{10EE} on resin (8.71 µmol), BCN_{10EE} was obtained as a red powder (1.00 mg, 8%). Analytical UPLC tr = 1.50 min; ESI-MS (negative mode) calculated for $[C_{68}H_{88}BN_{15}O_{25}]$, 1525.6; found m/z, 1525,1 (M − H)$^-$. [Focused gradient 34–44% of B in 15 min]. UV-Visible absorption spectrum and fluorescence excitation/emission spectra are given in Figure S33.

- BCN$_{11EE}$: Starting from P$_{11EE}$ on resin (8.71 μmol), BCN$_{11EE}$ was obtained as a red powder (1.01 mg, 11%). Analytical UPLC tr = 1.49 min; ESI-MS (negative mode) calculated for [C$_{72}$H$_{93}$BN$_{16}$O$_{28}$], 1640.6; found m/z, 1640.3 (M − H)$^-$. [Focused gradient 33–43% of B in 15 min].
- BCN$_{11SE}$: Starting from P$_{11SE}$ on resin (4.35 μmol), BCN$_{11SE}$ was obtained as a red powder (1.12 mg, 16%). Analytical UPLC tr = 1.48 min; ESI-MS (negative mode) calculated for [C$_{70}$H$_{91}$BN$_{16}$O$_{27}$], 1598.6; found m/z, 1598.2 (M − H)$^-$. [Focused gradient 32–42% of B in 15 min].

4.4.3. Fluorescein-Labeled F$_n$-Peptides

Due to reported instability of FTU-labelled peptides under acidic conditions [70], the coupling of FITC with synthesized P$_3$, P$_4$, P$_{5E}$, P$_{7E}$, P$_{9E}$, P$_{11SE}$, P$_{11EE}$ peptides and commercial pP$_{11}$ and P$_{11SS}$ peptides was performed in solution. FITC (2 equiv) was added to a solution of the peptides (1 equiv) and DIPEA (9 equiv) in anhydrous DMF (0.06 mL/mg peptide). Solutions were stirred for 30 min to 1h depending on the peptide. Solutions were then purified by HPLC on semi-preparative column using focused gradients and freeze dried. UPLC traces and analysis for F$_n$ peptides are given in Figures S12–S20.

- F$_3$: Starting from P$_3$ (5.00 mg, 9.55 μmol), F$_3$ was obtained as a yellow powder (3.00 mg, 48%). Analytical UPLC tr = 1.31 min; ESI-MS (negative mode) calculated for [C$_{39}$H$_{34}$N$_4$O$_{13}$S], 798.2; found m/z, 797.6 (M − H)$^-$. [Focused gradient 25–45% of B in 15 min].
- F$_4$: Starting from P$_4$ (5.00 mg, 7.85 μmol), F$_4$ was obtained as a yellow powder (4.30 mg, 62%). Analytical UPLC tr = 2.12 min; ESI-MS (negative mode) calculated for [C$_{45}$H$_{45}$N$_5$O$_{14}$S], 911.3; found m/z, 910.6 (M − H)$^-$. [Focused gradient 55–65% of solvent D consisted of MeOH containing 9.9% (v/v) H$_2$O and 0.1% TFA in 15 min].
- F$_{5E}$: Starting from P$_{5E}$ (5.00 mg, 6.53 μmol), F$_{5E}$ was obtained as a yellow powder (3.60 mg, 53%). Analytical UPLC tr = 0.98 min; ESI-MS (positive mode) calculated for [C$_{50}$H$_{52}$N$_6$O$_{17}$S], 1040.3; found m/z, 1041.8 (M + H)$^+$. [Focused gradient 35–45% of B in 15 min].
- F$_{7E}$: Starting from P$_{7E}$ (5.00 mg, 5.03 μmol), F$_{7E}$ was obtained as a yellow powder (2.60 mg, 50%). Analytical UPLC tr = 1.53 min; ESI-MS (positive mode) calculated for [C$_{60}$H$_{68}$N$_8$O$_{21}$S], 1268.4; found m/z, 1270.0 (M + H)$^+$. [Focused gradient 30–50% of B in 15 min].
- F$_{9E}$: Starting from P$_{9E}$ (5.00 mg, 4.09 μmol), F$_{9E}$ was obtained as a yellow powder (1.40 mg, 22%) Analytical UPLC tr = 1.42 min; ESI-MS (positive mode) calculated for [C$_{68}$H$_{79}$N$_{11}$O$_{26}$S], 1497.5; found m/z, 1499.7 (M + H)$^+$. [Focused gradient 30–50% of B in 15 min].
- F$_{11}$: Starting from commercial P$_{11}$ (4.30 mg, 3.11 μmol), F$_{11SS}$ was obtained as a yellow powder (3.5 mg, 68%). Analytical UPLC tr = 1.45 min; ESI-MS (positive mode) calculated for [C$_{73}$H$_{87}$N$_{13}$O$_{30}$S], 1657.5; found m/z, 1659.8 (M + H)$^+$. [Focused gradient 25–45% of B in 15 min].
- F$_{11SE}$: Starting from P$_{11SE}$ (4.50 mg, 3.43 μmol), F$_{11SE}$ was obtained as a yellow powder (0.90 mg, 15%). Analytical UPLC tr = 1.39 min; ESI-MS (negative mode) calculated for [C$_{75}$H$_{89}$N$_{13}$O$_{31}$S], 1699.6; found m/z, 1697.7 (M − H)$^-$. [Focused gradient 25–45% of B in 15 min].
- F$_{11EE}$: Starting from P$_{11EE}$ (5 mg, 3.41 μmol), F$_{11EE}$ was obtained as a yellow powder (2.40 mg, 40%). Analytical UPLC tr = 1.39 min; ESI-MS (positive mode) calculated for [C$_{77}$H$_{91}$N$_{13}$O$_{32}$S], 1741.6; found m/z, 1742.6 (M + H)$^+$. [Focused gradient 25–45% of B in 15 min].
- pF$_{11}$: Starting from commercial pP$_{11}$ (4.20 mg, 2.93 μmol), pF$_{11}$ was obtained as a yellow powder (1.10 mg, 20%). Analytical UPLC tr = 1.36 min; ESI-MS (negative mode) calculated for [C$_{73}$H$_{89}$N$_{13}$O$_{36}$P$_2$S], 1817.5; found m/z, 908.7 (M − 2H)$^{2-}$. [Focused gradient 25–45% of B in 15 min].

4.5. Bacterial Expression and Purification of RSV N Protein

Recombinant RSV N protein was produced in *E. coli* BL21(DE3) bacteria (Novagen, Madison, WI). The N-terminal domain N_{NTD} (residues 31–252), containing a C-terminal 6x histidine tag, was overexpressed using the pET-N(31–252) plasmid and purified as described previously [21]. In a final step N_{NTD} was dialyzed into MES 20 mM pH 6.5, NaCl 250 mM buffer [33]. Full-length N was produced by co-expression with the C-terminal domain of RSV P protein in *E. coli* BL21(DE3) co-transformed with pET-N and pGEX-P(161–241) plasmids [21]. Cultures were grown at 37 °C for 8 h in Luria-Bertani (LB) medium supplemented with 50 μg/mL kanamycin and 100 μg/mL ampicillin. An equivalent volume of LB was then added, and protein expression was induced with 80 μg/mL isopropyl-β-D-thio-galactoside (IPTG) for 15 h at 28 °C. Bacteria were harvested by centrifugation. The bacterial pellet was resuspended in lysis buffer (20 mM Tris-HCl pH 8.5, 150 mM NaCl, 1 mM EDTA, 2 mM dithiothreitol, 0.2% Triton X-100, 1 mg/mL lysozyme). Complete protease inhibitor cocktail (Roche, Mannheim, Germany) was added, and the suspension was incubated for 1 h on ice, sonicated and centrifuged at 4 °C for 30 min at $10,000 \times g$. Glutathione-Sepharose 4B beads (GE Healthcare, Vélizy-Villacoublay, France) were added to the clarified supernatant and incubated at 4 °C for 3 h. The beads were washed twice in lysis buffer and three times in 20 mM Tris-HCl pH 8.5, 150 mM NaCl buffer. GST was cleaved from the N-P(161–241) complex by treating the beads with thrombin (Novagen) for 16 h at 20 °C. The supernatant was then loaded onto a Superdex 200 16/30 column (GE Healthcare) and eluted in 20 mM Tris-HCl pH 8.5, 150 mM NaCl buffer. Finally, the fractions containing the N protein in the form of an N-RNA complex were pooled and concentrated up to 2 mg/mL (45 μM of N protein). The protein was subsequently dialyzed into 20 mM Tris pH 8.0 buffer containing 0.01% Brij-35. The concentration of N protein was determined with a BCA assay (Thermo Fisher, Illkirch-Graffenstaden, France), calibrated with BSA.

4.6. NMR Measurements

NMR titration experiments with ^{15}N-N_{NTD} were performed in 20 mM MES pH 6.5, 250 mM NaCl buffer. pP_{11} peptide was solubilized at 1 mg/mL in MQ water by addition of 1 M NaOH until the pH became neutral. pP_{11} aliquots were lyophilized. For the titration experiment, pP_{11} was added stepwise to a 50 μM ^{15}N-N_{NTD} solution, using 0.2–6.2 molar equivalents. NMR data were acquired on a 14.1 T (600 MHz ^1H frequency) Bruker Avance III NMR spectrometer equipped with a cryogenic TCI probe. A standard 2D ^1H-^{15}N HSQC spectrum was recorded for each titration point.

For titration with fluorescein, 0.5–8 molar equivalents of fluorescein were added from a 10 mM stock solution in water at pH 6.5 to 55 μM ^{15}N-N_{NTD}. NMR measurements were performed on a 16.4 T (700 MHz ^1H frequency) Bruker NMR spectrometer equipped with a NEO console and a cryoTXO probe. All samples contained 7.5% ^2H_2O to lock the spectrometer frequency and 100 μM DSS to reference ^1H chemical shifts. The temperature was set to 20 °C. NMR data were processed with TopSpin 4.0 (Bruker Biospin, Wissembourg, France) and analyzed with CcpNmr Analysis 2.4 software [71]. Backbone chemical shift assignment of N_{NTD} was done previously [33].

Combined amide ^1H and ^{15}N chemical shift perturbations $\Delta\delta_{HN}$ were calculated with a scaling factor of 1/10 for ^{15}N, which corresponds to the ratio of ^{15}N and ^1H gyromagnetic ratios (Equation (1)):

$$\Delta\delta_{HN} = \sqrt{\left(\left(\delta^1H - \delta^1H_{ref}\right)^2 + \left(\delta^{15}N - \delta^{15}N_{ref}\right)^2/100\right)} \tag{1}$$

^1H and/or ^{15}N chemical shift perturbations were fitted in CcpNmr Analysis 2.4 as a function of the molar ligand:N_{NTD} ratio r, using a single binding site model with a 1:1 stoichiometry, and assuming a fast chemical exchange regime (Equation (2)). K_d is the

dissociation constant of the complex with N_{NTD}. δ_{free} and δ_{bound} (in ppm) are the chemical shifts of free and bound N_{NTD}.

$$(\delta - \delta_{ref}) = \frac{1}{2}(\delta_{bound} - \delta_{free}) \times \left(\frac{K_d}{[N_{NTD}]_{tot}} + 1 + r - \sqrt{\left(\frac{K_d}{[N_{NTD}]_{tot}} + 1 + r \right)^2 - 4r} \right) \tag{2}$$

For residues in intermediate exchange regime, the exchange rate between free and bound protein states k_{ex} (s^{-1}) was estimated according to Equation (3), where BF is the Larmor frequency (MHz) of the observed nucleus.

$$k_{ex} = \pi \times \Delta v = \pi \times (\delta_{bound} - \delta_{free}) \times BF \tag{3}$$

4.7. Fluorescence Polarization Measurements

Fluorescence polarization measurements were carried out on a Paradigm Detection Platform (Beckman Coulter, Brea, CA, USA) operating with a microplate reader, a fluorescein detection cartridge (excitation range 485/20 nm, emission range 535/25 nm for both parallel and perpendicular components) and the SpectraMax Pro 6.1 software (Molecular Devices, San Jose, CA, USA). Samples were placed in polystyrene black flat bottom 96-well microplates (Cellstar, Greiner bio-one, Frickenhausen, Germany) with 20 µL final volume in each well. If not stated otherwise, the final concentration of fluorescent ligands was 200 nM. The buffer was either 20 mM MES pH 6.5, salt-free or with 250 mM NaCl, or 20 mM Tris pH 8.0 salt-free or with 100 mM NaCl, supplemented with 0.01% Brij-35. Mixing was done using the corresponding plate reader option. The temperature was set to 20 °C. Data were recorded in top reading mode. Measurements were done in triplicate and after an incubation time of 30 min, if not indicated otherwise. Fluorescence polarization (FP) in mFP units was determined from the parallel ($I_{\parallel}$) and perpendicular ($I_{\perp}$) components of the emitted light according to Equation (4) [43]. A grating factor G of 1.2 was determined using 1 nM fluorescein in 1 mM NaOH and assuming a theoretical FP of 27 mFP [48]. Background signal was measured from wells containing only buffer, and the mean value was subtracted from each $I_{\parallel}$ and $I_{\perp}$ component.

$$FP\,(mP) = 1000 \times \left(I_{\parallel} - G * I_{\perp} \right) / \left(I_{\parallel} + G \times I_{\perp} \right) \tag{4}$$

Theoretical fluorescence polarization values of a fluorophore bound to N protein were calculated from the fluorescence lifetime τ and the molecular weight MW using Perrin's equation (Equation (5)). A is the fluorescence anisotropy related to FP by Equation (6) [43], A_0 the intrinsic anisotropy (0.4), T the temperature in Kelvin, k the Planck constant, η the dynamic viscosity, and V_h the hydrated volume. V_h was calculated according to Equation (7), where N is the Avogadro number, v_2 the partial specific volume of the protein (7.34×10^{-7} m^3/g), δ the degree of hydration (0.75), and v_1^0 the specific volume of water (10^{-6} m^3/g). We used A_0, v_2, δ and v_1^0 values reported for bovine serum albumine [72].

$$A = A_0 / \left(1 + \frac{kT \times \tau}{\eta * V_h} \right) \tag{5}$$

$$FP = 1000 \times 3A / (2 + A) \tag{6}$$

$$V_h = (MW/N) \times \left(v_2 + \delta \times v_1^0 \right) \tag{7}$$

We assumed that the measured fluorescence polarization FP is a linear combination of the FP of the fluorescent probe in the absence of N protein (FP_{min}) and the FP of N-bound fluorescent probe (FP_{max}), weighted by the molar fraction. The molar fraction $x = [P]_{bound}/[P]_0$ can then be expressed as a ratio of FP differences (Equation (8)).

$$x = (FP - FP_{min}) / (FP_{max} - FP_{min}) = \Delta FP / \Delta FP_{max} \tag{8}$$

To determine the K_d value of a complex between a fluorescent probe and N protein, a series of samples with constant probe concentration and varying N concentration was measured. FP binding curves were fitted with a single binding site model and a 1:1 stoichiometry. The molar fraction of bound fluorescent probe was expressed as a function of the ratio of protein versus probe concentrations, $r = [N]_0/[P]_0$, according to Equation (9). Binding curves were fitted in Origin 7 software according to Equation (10), obtained by combining Equations (8) and (9).

$$x = 0.5 \times \left[1 + r + K_d/[P]_0 - \sqrt{(1 + r + K_d/[P]_0)^2 - 4r} \right] \tag{9}$$

$$\Delta FP = 0.5 \times \Delta FP_{max} \times \left[1 + r + K_d/[P]_0 + \sqrt{(1 + r + K_d/[P]_0)^2 - 4r} \right] \tag{10}$$

To assess inhibition of a complex between a fluorescent probe and N protein by peptides or the M76 molecule, the concentration of N was set to work with an FP range comprised between FP_{min} and ~80% FP_{max}. Peptides were added from 1 or 2 mM stock solution in water at neutral pH. M76 was added from 10 or 20 mM stock solutions in ethanol or in DMSO. The percentage of inhibition ($\%_i$) was calculated as the relative change in FP (Equation (11)). $\%_i$ was fitted as a function of inhibitor concentration with a Hill equation, where IC_{50} is the inhibitor concentration resulting in 50% inhibition (Equation (12)). Inhibition data were fitted with Origin 7, and in parallel with the Excel solver module. All data were compatible with an absence of cooperativity. FP_{max} and FP_{min} were fitted, and the maximal inhibition $\%_{i,max}$ was set to 100%.

$$\%_i = 100 \times [1 - (FP - FP_{min})/(FP_{max} - FP_{min})] \tag{11}$$

$$\%_i = \%_{i,max} \times \frac{[\text{inhibitor}]}{[\text{inhibitor}] + IC_{50}} \tag{12}$$

Inhibition constants K_i were calculated on the IC50-to-Ki converter for a protein-ligand-inhibitor system (https://bioinfo-abcc.ncifcrf.gov/IC50_Ki_Converter/index.php, accessed on 24 August 2022) [49], assuming a competitive mechanism (Equation (13)). This tool takes into account the free concentrations of protein and ligand.

$$K_i = \left(IC_{50} - \frac{[\text{protein}]}{2} \right) / \left(\frac{[\text{peptide}]}{K_d} + 1 \right) \tag{13}$$

A Z′-factor for FP measurements without test compound [58] was calculated from 7 data points for the condition 200 nM B_{10EE} and 1 μM N-RNA, using Equation (14), where σ_+ and σ_- are the standard deviations of positive (fluorescent peptide bound to N protein) and negative (free fluorescent peptide) controls, respectively, and μ_+ and μ_- their mean values.

$$Z' = 1 - (3\sigma_+ + 3\sigma_-)/|\mu_+ - \mu_-| \tag{14}$$

4.8. Complex Modelling with Haddock

Docking of the P_{11} peptide onto N_{NTD} was performed with the Haddock 2.4 software [65] on the WeNMR server [73]. A structure of P_{11} was built with the PEP-FOLD3 server [64] and allowed to be flexible (residues 1–9) during docking. The C-terminal Asp_{10} and Phe_{11} residues (equivalent to Asp_{240} and Phe_{241}) were declared as active residues. The structure of N_{NTD} was extracted from the X-ray structure of the N_{NTD}-P_2 complex (PDB 4uc9). N residues 46, 50, 53, 128, 131, 132, 135, 145, and 151, lining the P-binding pocket, were declared as active residues. Passive residues were automatically defined around active residues. Default scoring parameters for protein–protein complexes were used, except for Evdw 1, which was increased from 0.01 to 1. 1000 initial structures were generated. 200 final structures were refined in water and clustered according to the RMSD criterion. Haddock clustered 156 structures in 12 clusters. Cluster 1 with the best haddock score (-96.4 ± 4.9) contained 63 structures, i.e., 40% of clustered structures.

4.9. Docking of Small Compounds

Fluorescein and fluorescein methyl ester were docked on the P-binding pocket of N_{NTD} (PDB 4ucc) using Smina software and MOE [53]. For Smina, Vinardo [54] scoring function was selected with an exhaustiveness of 8. The pose with the best scoring value was retained. For MOE, the placement method used was Triangle Matcher with London dG score and the number of poses was set to 30. These poses were then refined with GBVI/WSA dG score with rigid receptor, and the number of output poses was set to 5. The pose with the best GBVI/WSA dG score was retained.

References

1. O'Brien, K.L.; Baggett, H.C.; Brooks, W.A.; Feikin, D.R.; Hammitt, L.L.; Higdon, M.M.; Howie, S.R.; Knoll, M.D.; Kotloff, K.L.; Levine, O.S.; et al. Causes of severe pneumonia requiring hospital admission in children without HIV infection from Africa and Asia: The PERCH multi-country case-control study. *Lancet* **2019**, *394*, 757–779. [CrossRef] [PubMed]
2. Shi, T.; McAllister, D.A.; O'Brien, K.L.; Simoes, E.A.F.; Madhi, S.A.; Gessner, B.D.; Polack, F.P.; Balsells, E.; Acacio, S.; Aguayo, C.; et al. Global, regional, and national disease burden estimates of acute lower respiratory infections due to respiratory syncytial virus in young children in 2015: A systematic review and modelling study. *Lancet* **2017**, *390*, 946–958. [CrossRef] [PubMed]
3. Nair, H.; Nokes, D.J.; Gessner, B.D.; Dherani, M.; Madhi, S.A.; Singleton, R.J.; O'Brien, K.L.; Roca, A.; Wright, P.F.; Bruce, N.; et al. Global burden of acute lower respiratory infections due to respiratory syncytial virus in young children: A systematic review and meta-analysis. *Lancet* **2010**, *375*, 1545–1555. [CrossRef] [PubMed]
4. Coultas, J.A.; Smyth, R.; Openshaw, P.J. Respiratory syncytial virus (RSV): A scourge from infancy to old age. *Thorax* **2019**, *74*, 986–993. [CrossRef] [PubMed]
5. Cockerill, G.S.; Good, J.A.D.; Mathews, N. State of the Art in Respiratory Syncytial Virus Drug Discovery and Development. *J. Med. Chem.* **2019**, *62*, 3206–3227. [CrossRef]
6. Elawar, F.; Oraby, A.K.; Kieser, Q.; Jensen, L.D.; Culp, T.; West, F.G.; Marchant, D.J. Pharmacological targets and emerging treatments for respiratory syncytial virus bronchiolitis. *Pharmacol. Ther.* **2021**, *220*, 107712. [CrossRef]
7. Griffiths, C.; Drews, S.J.; Marchant, D.J. Respiratory Syncytial Virus: Infection, Detection, and New Options for Prevention and Treatment. *Clin. Microbiol. Rev.* **2017**, *30*, 277–319. [CrossRef]
8. Hammitt, L.L.; Dagan, R.; Yuan, Y.; Baca Cots, M.; Bosheva, M.; Madhi, S.A.; Muller, W.J.; Zar, H.J.; Brooks, D.; Grenham, A.; et al. Nirsevimab for Prevention of RSV in Healthy Late-Preterm and Term Infants. *N. Engl. J. Med.* **2022**, *386*, 837–846. [CrossRef]
9. Thornhill, E.M.; Salpor, J.; Verhoeven, D. Respiratory syntycial virus: Current treatment strategies and vaccine approaches. *Antivir. Chem. Chemother.* **2020**, *28*, 2040206620947303. [CrossRef]
10. Mazur, N.I.; Terstappen, J.; Baral, R.; Bardají, A.; Beutels, P.; Buchholz, U.J.; Cohen, C.; Crowe, J.E.; Cutland, C.L.; Eckert, L.; et al. Respiratory syncytial virus prevention within reach: The vaccine and monoclonal antibody landscape. *Lancet Infect. Dis.* **2022**, *23*, e2–e21. [CrossRef]

11. Heylen, E.; Neyts, J.; Jochmans, D. Drug candidates and model systems in respiratory syncytial virus antiviral drug discovery. *Biochem. Pharmacol.* **2017**, *127*, 1–12. [CrossRef]

12. Nicholson, E.G.; Munoz, F.M. A Review of Therapeutics in Clinical Development for Respiratory Syncytial Virus and Influenza in Children. *Clin. Ther.* **2018**, *40*, 1268–1281. [CrossRef]

13. Stevens, M.; Rusch, S.; DeVincenzo, J.; Kim, Y.-I.; Harrison, L.; Meals, E.A.; Boyers, A.; Fok-Seang, J.; Huntjens, D.; Lounis, N.; et al. Antiviral Activity of Oral JNJ-53718678 in Healthy Adult Volunteers Challenged with Respiratory Syncytial Virus: A Placebo-Controlled Study. *J. Infect. Dis.* **2018**, *218*, 748–756. [CrossRef]

14. DeVincenzo, J.P.; Whitley, R.J.; Mackman, R.L.; Scaglioni-Weinlich, C.; Harrison, L.; Farrell, E.; McBride, S.; Lambkin-Williams, R.; Jordan, R.; Xin, Y.; et al. Oral GS-5806 activity in a respiratory syncytial virus challenge study. *N. Engl. J. Med.* **2014**, *371*, 711–722. [CrossRef]

15. Detalle, L.; Stohr, T.; Palomo, C.; Piedra, P.A.; Gilbert, B.E.; Mas, V.; Millar, A.; Power, U.F.; Stortelers, C.; Allosery, K.; et al. Generation and Characterization of ALX-0171, a Potent Novel Therapeutic Nanobody for the Treatment of Respiratory Syncytial Virus Infection. *Antimicrob. Agents Chemother.* **2016**, *60*, 6–13. [CrossRef]

16. DeVincenzo, J.P.; McClure, M.W.; Symons, J.A.; Fathi, H.; Westland, C.; Chanda, S.; Lambkin-Williams, R.; Smith, P.; Zhang, Q.; Beigelman, L.; et al. Activity of Oral ALS-008176 in a Respiratory Syncytial Virus Challenge Study. *N. Engl. J. Med.* **2015**, *373*, 2048–2058. [CrossRef]

17. Amarasinghe, G.K.; Ayllon, M.A.; Bao, Y.; Basler, C.F.; Bavari, S.; Blasdell, K.R.; Briese, T.; Brown, P.A.; Bukreyev, A.; Balkema-Buschmann, A.; et al. Taxonomy of the order Mononegavirales: Update 2019. *Arch. Virol.* **2019**, *164*, 1967–1980. [CrossRef]

18. Collins, P.L.; Karron, R.A. Respiratory Syncytial Virus and Metapneumovirus. In *Fields Virology*, 6th ed.; Knipe, D.M., Howley, P.M., Eds.; Lippinscot Williams & Wilkins, Wolters Kluwer: Philadelphia, PA, USA, 2013; pp. 1086–1123.

19. Collins, P.L.; Melero, J.A. Progress in understanding and controlling respiratory syncytial virus: Still crazy after all these years. *Virus Res.* **2011**, *162*, 80–99. [CrossRef] [PubMed]

20. Bakker, S.E.; Duquerroy, S.; Galloux, M.; Loney, C.; Conner, E.; Eleouet, J.F.; Rey, F.A.; Bhella, D. The respiratory syncytial virus nucleoprotein-RNA complex forms a left-handed helical nucleocapsid. *J. Gen. Virol.* **2013**, *94*, 1734–1738. [CrossRef]

21. Galloux, M.; Tarus, B.; Blazevic, I.; Fix, J.; Duquerroy, S.; Eleouet, J.F. Characterization of a viral phosphoprotein binding site on the surface of the respiratory syncytial nucleoprotein. *J. Virol.* **2012**, *86*, 8375–8387. [CrossRef]

22. Fearns, R. The Respiratory Syncytial Virus Polymerase: A Multitasking Machine. *Trends Microbiol.* **2019**, *27*, 969–971. [CrossRef] [PubMed]

23. Gilman, M.S.A.; Liu, C.; Fung, A.; Behera, I.; Jordan, P.; Rigaux, P.; Ysebaert, N.; Tcherniuk, S.; Sourimant, J.; Eleouet, J.F.; et al. Structure of the Respiratory Syncytial Virus Polymerase Complex. *Cell* **2019**, *179*, 193–204 e114. [CrossRef] [PubMed]

24. Galloux, M.; Risso-Ballester, J.; Richard, C.A.; Fix, J.; Rameix-Welti, M.A.; Eleouet, J.F. Minimal Elements Required for the Formation of Respiratory Syncytial Virus Cytoplasmic Inclusion Bodies In Vivo and In Vitro. *MBio* **2020**, *11*, e01202-20. [CrossRef] [PubMed]

25. Lakdawala, S.; Lopez, N.; Camporeale, G.; Salgueiro, M.; Borkosky, S.S.; Visentín, A.; Peralta-Martinez, R.; Loureiro, M.E.; de Prat-Gay, G. Deconstructing virus condensation. *PLoS Pathog.* **2021**, *17*, e1009926. [CrossRef]

26. Pereira, N.; Cardone, C.; Lassoued, S.; Galloux, M.; Fix, J.; Assrir, N.; Lescop, E.; Bontems, F.; Eleouet, J.F.; Sizun, C. New Insights into Structural Disorder in Human Respiratory Syncytial Virus Phosphoprotein and Implications for Binding of Protein Partners. *J. Biol. Chem.* **2017**, *292*, 2120–2131. [CrossRef]

27. Cardone, C.; Caseau, C.-M.; Bardiaux, B.; Thureaux, A.; Galloux, M.; Bajorek, M.; Eléouët, J.-F.; Litaudon, M.; Bontems, F.; Sizun, C. A Structural and Dynamic Analysis of the Partially Disordered Polymerase-Binding Domain in RSV Phosphoprotein. *Biomolecules* **2021**, *11*, 1225. [CrossRef]

28. Noval, M.G.; Esperante, S.A.; Molina, I.G.; Chemes, L.B.; Prat-Gay, G. Intrinsic disorder to order transitions in the scaffold phosphoprotein P from the respiratory syncytial virus RNA-polymerase complex. *Biochemistry* **2016**, *55*, 1441–1454. [CrossRef]

29. Cardone, C.; Caseau, C.-M.; Pereira, N.; Sizun, C. Pneumoviral Phosphoprotein, a Multidomain Adaptor-Like Protein of Apparent Low Structural Complexity and High Conformational Versatility. *Int. J. Mol. Sci.* **2021**, *22*, 1537. [CrossRef]

30. Galloux, M.; Gabiane, G.; Sourimant, J.; Richard, C.A.; England, P.; Moudjou, M.; Aumont-Nicaise, M.; Fix, J.; Rameix-Welti, M.A.; Eleouet, J.F. Identification and characterization of the binding site of the respiratory syncytial virus phosphoprotein to RNA-free nucleoprotein. *J. Virol.* **2015**, *89*, 3484–3496. [CrossRef]

31. Tran, T.L.; Castagne, N.; Bhella, D.; Varela, P.F.; Bernard, J.; Chilmonczyk, S.; Berkenkamp, S.; Benhamo, V.; Grznarova, K.; Grosclaude, J.; et al. The nine C-terminal amino acids of the respiratory syncytial virus protein P are necessary and sufficient for binding to ribonucleoprotein complexes in which six ribonucleotides are contacted per N protein protomer. *J. Gen. Virol.* **2007**, *88*, 196–206. [CrossRef]

32. Tawar, R.G.; Duquerroy, S.; Vonrhein, C.; Varela, P.F.; Damier-Piolle, L.; Castagne, N.; MacLellan, K.; Bedouelle, H.; Bricogne, G.; Bhella, D.; et al. Crystal structure of a nucleocapsid-like nucleoprotein-RNA complex of respiratory syncytial virus. *Science* **2009**, *326*, 1279–1283. [CrossRef]

33. Ouizougun-Oubari, M.; Pereira, N.; Tarus, B.; Galloux, M.; Lassoued, S.; Fix, J.; Tortorici, M.A.; Hoos, S.; Baron, B.; England, P.; et al. A Druggable Pocket at the Nucleocapsid/Phosphoprotein Interaction Site of Human Respiratory Syncytial Virus. *J. Virol.* **2015**, *89*, 11129–11143. [CrossRef]

34. Tompa, P.; Fuxreiter, M. Fuzzy complexes: Polymorphism and structural disorder in protein-protein interactions. *Trends Biochem. Sci.* **2008**, *33*, 2–8. [CrossRef]

35. Sharma, R.; Raduly, Z.; Miskei, M.; Fuxreiter, M. Fuzzy complexes: Specific binding without complete folding. *FEBS Lett.* **2015**, *589*, 2533–2542. [CrossRef]

36. Mazumder, B.; Barik, S. Requirement of casein kinase II-mediated phosphorylation for the transcriptional activity of human respiratory syncytial viral phosphoprotein P: Transdominant negative phenotype of phosphorylation-defective P mutants. *Virology* **1994**, *205*, 104–111. [CrossRef]

37. Sanchez-Seco, M.P.; Navarro, J.; Martinez, R.; Villanueva, N. C-terminal phosphorylation of human respiratory syncytial virus P protein occurs mainly at serine residue 232. *J. Gen. Virol.* **1995**, *76 Pt. 2*, 425–430. [CrossRef]

38. Villanueva, N.; Hardy, R.; Asenjo, A.; Yu, Q.; Wertz, G. The bulk of the phosphorylation of human respiratory syncytial virus phosphoprotein is not essential but modulates viral RNA transcription and replication. *J. Gen. Virol.* **2000**, *81*, 129–133. [CrossRef]

39. Lu, B.; Ma, C.H.; Brazas, R.; Jin, H. The major phosphorylation sites of the respiratory syncytial virus phosphoprotein are dispensable for virus replication in vitro. *J. Virol.* **2002**, *76*, 10776–10784. [CrossRef]

40. Kaul, T.N.; Middleton, E.; Ogra, P.L. Antiviral effect of flavonoids on human viruses. *J. Med. Virol.* **1985**, *15*, 71–79. [CrossRef]

41. Sa, J.M.; Piloto, J.V.; Cilli, E.M.; Tasic, L.; Fossey, M.A.; Almeida, F.C.L.; Souza, F.P.; Caruso, I.P. Hesperetin targets the hydrophobic pocket of the nucleoprotein/phosphoprotein binding site of human respiratory syncytial virus. *J. Biomol. Struct. Dyn.* **2020**, *40*, 2156–2168. [CrossRef]

42. Rhodin, M.H.J.; McAllister, N.V.; Castillo, J.; Noton, S.L.; Fearns, R.; Kim, I.J.; Yu, J.; Blaisdell, T.P.; Panarese, J.; Shook, B.C.; et al. EDP-938, a novel nucleoprotein inhibitor of respiratory syncytial virus, demonstrates potent antiviral activities in vitro and in a non-human primate model. *PLoS Pathog.* **2021**, *17*, e1009428. [CrossRef] [PubMed]

43. Lakowicz, J.R. Fluorescence Anisotropy. In *Principles of Fluorescence Spectroscopy*; Kluwer Academic/Plenum Publisher: New York, NY, USA, 1999; pp. 291–319. [CrossRef]

44. Zhang, H.; Wu, Q.; Berezin, M.Y. Fluorescence anisotropy (polarization): From drug screening to precision medicine. *Expert Opin. Drug Discov.* **2015**, *10*, 1145–1161. [CrossRef] [PubMed]

45. Shapiro, A.B.; Gao, N.; O'Connell, N.; Hu, J.; Thresher, J.; Gu, R.F.; Overman, R.; Hardern, I.M.; Sproat, G.G. Quantitative investigation of the affinity of human respiratory syncytial virus phosphoprotein C-terminus binding to nucleocapsid protein. *Virol. J.* **2014**, *11*, 191. [CrossRef] [PubMed]

46. Xie, Y.; Jiang, Y.; Ben-Amotz, D. Detection of amino acid and peptide phosphate protonation using Raman spectroscopy. *Anal. Biochem.* **2005**, *343*, 223–230. [CrossRef] [PubMed]

47. Sportsman, J.R. Fluorescence anisotropy in pharmacologic screening. *Methods Enzymol.* **2003**, *361*, 505–529. [CrossRef]

48. Hall, M.D.; Yasgar, A.; Peryea, T.; Braisted, J.C.; Jadhav, A.; Simeonov, A.; Coussens, N.P. Fluorescence polarization assays in high-throughput screening and drug discovery: A review. *Methods Appl. Fluoresc.* **2016**, *4*, 022001. [CrossRef]

49. Cer, R.Z.; Mudunuri, U.; Stephens, R.; Lebeda, F.J. IC50-to-Ki: A web-based tool for converting IC50 to Ki values for inhibitors of enzyme activity and ligand binding. *Nucleic Acids Res.* **2009**, *37*, W441–W445. [CrossRef]

50. Martin, M.M.; Lindqvist, L. The pH dependence of fluorescein fluorescence. *J. Lumin.* **1975**, *10*, 381–390. [CrossRef]

51. Klonis, N.; Sawyer, W.H. Spectral properties of the prototropic forms of fluorescein in aqueous solution. *J. Fluoresc.* **1996**, *6*, 147–157. [CrossRef]

52. Le Guern, F.; Mussard, V.; Gaucher, A.; Rottman, M.; Prim, D. Fluorescein Derivatives as Fluorescent Probes for pH Monitoring along Recent Biological Applications. *Int. J. Mol. Sci.* **2020**, *21*, 9217. [CrossRef]

53. Chemical Computing Group. *Molecular Operating Environment (MOE)*; Chemical Computing Group ULC: Montreal, QC, Canada, 2022.

54. Quiroga, R.; Villarreal, M.A. Vinardo: A Scoring Function Based on Autodock Vina Improves Scoring, Docking, and Virtual Screening. *PLoS ONE* **2016**, *11*, e0155183. [CrossRef]

55. Uriel, C.; Gómez, A.M.; García Martínez de la Hidalga, E.; Bañuelos, J.; Garcia-Moreno, I.; López, J.C. Access to 2,6-Dipropargylated BODIPYs as "Clickable" Congeners of Pyrromethene-567 Dye: Photostability and Synthetic Versatility. *Org. Lett.* **2021**, *23*, 6801–6806. [CrossRef]

56. Blázquez-Moraleja, A.; Maierhofer, L.; Mann, E.; Prieto-Montero, R.; Oliden-Sánchez, A.; Celada, L.; Martínez-Martínez, V.; Chiara, M.-D.; Chiara, J.L. Acetoxymethyl-BODIPY dyes: A universal platform for the fluorescent labeling of nucleophiles. *Org. Chem. Front.* **2022**, *9*, 5774–5789. [CrossRef]

57. Moerke, N.J. Fluorescence Polarization (FP) Assays for Monitoring Peptide-Protein or Nucleic Acid-Protein Binding. *Curr. Protoc. Chem. Biol.* **2009**, *1*, 1–15. [CrossRef]

58. Zhang, J.-H.; Chung, T.D.Y.; Oldenburg, K.R. A Simple Statistical Parameter for Use in Evaluation and Validation of High Throughput Screening Assays. *SLAS Discov.* **1999**, *4*, 67–73. [CrossRef]

59. Liu, H.; Shen, L.; Pan, C.; Huang, W. Structural modeling, energetic analysis and molecular design of a π-stacking system at the complex interface of pediatric respiratory syncytial virus nucleocapsid with the C-terminal peptide of phosphoprotein. *Biophys. Chem.* **2023**, *292*, 106916. [CrossRef]

60. Collins, P.L.; Fearns, R.; Graham, B.S. Respiratory Syncytial Virus: Virology, Reverse Genetics, and Pathogenesis of Disease. In *Challenges and Opportunities for Respiratory Syncytial Virus Vaccines*; Springer: Berlin/Heidelberg, Germany, 2013; pp. 3–38. [CrossRef]

61. Schobel, S.A.; Stucker, K.M.; Moore, M.L.; Anderson, L.J.; Larkin, E.K.; Shankar, J.; Bera, J.; Puri, V.; Shilts, M.H.; Rosas-Salazar, C.; et al. Respiratory Syncytial Virus whole-genome sequencing identifies convergent evolution of sequence duplication in the C-terminus of the G gene. *Sci. Rep.* **2016**, *6*, 26311. [CrossRef]

62. Chapman, J.; Abbott, E.; Alber, D.G.; Baxter, R.C.; Bithell, S.K.; Henderson, E.A.; Carter, M.C.; Chambers, P.; Chubb, A.; Cockerill, G.S.; et al. RSV604, a novel inhibitor of respiratory syncytial virus replication. *Antimicrob. Agents Chemother.* **2007**, *51*, 3346–3353. [CrossRef]

63. Challa, S.; Scott, A.D.; Yuzhakov, O.; Zhou, Y.; Tiong-Yip, C.L.; Gao, N.; Thresher, J.; Yu, Q. Mechanism of action for respiratory syncytial virus inhibitor RSV604. *Antimicrob. Agents Chemother.* **2015**, *59*, 1080–1087. [CrossRef]

64. Lamiable, A.; Thevenet, P.; Rey, J.; Vavrusa, M.; Derreumaux, P.; Tuffery, P. PEP-FOLD3: Faster de novo structure prediction for linear peptides in solution and in complex. *Nucleic Acids Res.* **2016**, *44*, W449–W454. [CrossRef]

65. van Zundert, G.C.P.; Rodrigues, J.; Trellet, M.; Schmitz, C.; Kastritis, P.L.; Karaca, E.; Melquiond, A.S.J.; van Dijk, M.; de Vries, S.J.; Bonvin, A. The HADDOCK2.2 Web Server: User-Friendly Integrative Modeling of Biomolecular Complexes. *J. Mol. Biol.* **2016**, *428*, 720–725. [CrossRef] [PubMed]

66. Rocchia, W.; Alexov, E.; Honig, B. Extending the applicability of the nonlinear Poisson-Boltzmann equation: Multiple dielectric constants and multivalent ions. *J. Phys. Chem. B* **2001**, *105*, 6507–6514. [CrossRef]

67. Lu, D.; Teng, F.; Liu, Y.; Lu, L.; Chen, C.; Lei, J.; Wang, L.; Zhang, J. Self-assembly of magnetically recoverable ratiometric Cu^{2+} fluorescent sensor and adsorbent. *RSC Adv.* **2014**, *4*, 18660–18667. [CrossRef]

68. Ng, C.Y.; Kwok, T.X.W.; Tan, F.C.K.; Low, C.-M.; Lam, Y. Fluorogenic probes to monitor cytosolic phospholipase A2 activity. *Chem. Commun.* **2017**, *53*, 1813–1816. [CrossRef]

69. Gießler, K.; Griesser, H.; Göhringer, D.; Sabirov, T.; Richert, C. Synthesis of 3′-BODIPY-Labeled Active Esters of Nucleotides and a Chemical Primer Extension Assay on Beads. *Eur. J. Org. Chem.* **2010**, *2010*, 3611–3620. [CrossRef]

70. Jullian, M.; Hernandez, A.; Maurras, A.; Puget, K.; Amblard, M.; Martinez, J.; Subra, G. N-terminus FITC labeling of peptides on solid support: The truth behind the spacer. *Tetrahedron Lett.* **2009**, *50*, 260–263. [CrossRef]

71. Vranken, W.F.; Boucher, W.; Stevens, T.J.; Fogh, R.H.; Pajon, A.; Llinas, M.; Ulrich, E.L.; Markley, J.L.; Ionides, J.; Laue, E.D. The CCPN data model for NMR spectroscopy: Development of a software pipeline. *Proteins* **2005**, *59*, 687–696. [CrossRef]

72. Gonzalez Flecha, F.L.; Levi, V. Determination of the molecular size of BSA by fluorescence anisotropy. *Biochem. Mol. Biol. Educ.* **2003**, *31*, 319–322. [CrossRef]

73. Honorato, R.V.; Koukos, P.I.; Jiménez-García, B.; Tsaregorodtsev, A.; Verlato, M.; Giachetti, A.; Rosato, A.; Bonvin, A.M.J.J. Structural Biology in the Clouds: The WeNMR-EOSC Ecosystem. *Front. Mol. Biosci.* **2021**, *8*, 708. [CrossRef]